ABSTRACT

Title of thesis: NUMERICAL AND EXPERIMENTAL STUDIES ON FREE PISTON STIRLING ENGINES

Dibesh Shrestha, 2012

Thesis directed by: Professor Balakumar Balachandran
Department of Mechanical Engineering

Free piston Stirling engine (FPSE) is a closed cycle engine that converts thermal energy into mechanical energy. The focus of this thesis is on understanding limit-cycle motions in FPSEs. First, making use of reduced-order models, parametric studies are carried out to understand what FPSE parameters affect the creation of oscillatory motions. It is shown that quasi-static variations of the stiffness and the damping terms on the power piston can lead to conditions for Hopf instabilities in the system. The effect of the inclusion of a nonlinear spring term to the system is also investigated through numerical studies. The nonlinear springs include hardening springs and magnetic springs. The results, which include first results for FPSEs with hardening springs, show that nonlinear springs can help these systems realize limit-cycle motions. Finally, preliminary experimental studies conducted to realize oscillatory motions in a FPSE with a magnetic spring are also reported.

NUMERICAL AND EXPERIMENTAL STUDIES ON FREE PISTON STIRLING ENGINES

by

Dibesh Shrestha

Thesis submitted to the Faculty of the Graduate School of the
University of Maryland, College Park, in partial fulfillment
of the requirements for the degree of
Master of Science
2012

Advisory Committee:
Professor Balakumar Balachandran, Chair and Advisor
Professor Amr Baz, Department of Mechanical Engineering
Assistant Professor Nikhil Chopra, Department of Mechanical Engineering

Acknowledgments

I would like to thank Professor Balachandran, my advisor and committee chair, for his support and guidance during my undergraduate and graduate studies. I would also like to thank my committee members, Professor Baz and Professor Chopra, for their assistance in completing this thesis.

I want to thank Vince Nguyen for aiding me in my research. I also want to thank all of my other colleagues in the Dynamics and Vibrations Group for their support and help. Finally, I would like to thank my family and friends for their support and love.

Table of Contents

List of Figures

Chapter 1

Introduction

The Stirling engine, invented by Robert Stirling in 1816, is a device that can be used to convert thermal energy into mechanical energy by taking advantage of the pressure variations within the system developed through a temperature gradient. This is a closed cycle regenerative engine, which compresses a fixed amount of gas through cooling and then expands the gas again through heating; this process is repeated cyclically. A schematic of an alpha type Stirling engine is shown in Figure 1.1, which shows the components of a Stirling engine. In order to create the temperature gradient, the working space of the engine is separated into two different compartments: the compression space where the working gas is cooled, and the expansion space where the working fluid is heated. Other necessary components for a Stirling engine are a cooling source to cool the fluid in the compression space, a heating source to heat the expansion space, a displacer piston, and a power piston. The main purpose of the pistons are to move the working fluid back and forth between the two compartments, which is further explained later in this chapter. Adding a regenerator, which acts as a heat exchanger, is said to increase the efficiency of a Stirling engine. A regenerator retains heat from the working fluid and then redelivers the heat again to the fluid as the fluid travels back and forth between the two compartments (Organ, 1992). The placement of the various components of

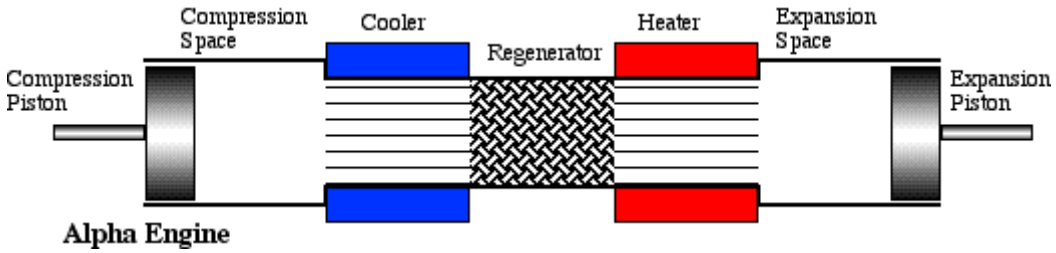

Figure 1.1: An example of Stirling engine configuration. (Source: Urieli, 2010)

the Stirling engine define the type of Stirling engine, which will be also discussed further in this chapter.

1.1 Configurations of Stirling Engines

Stirling engines can be classified on the basis of their driving mechanisms, namely, constrained drive systems such as kinematic Stirling engines and unconstrained drive systems like Free Piston Stirling engines (FPSE). Schematics for the kinematic Stirling engine and FPSE are shown in Figure 1.2. As shown in Figure 1.2(a), the motions of the kinematic Stirling engines are defined by the crankshafts and the rods that connect the power piston and the displacer. The power piston

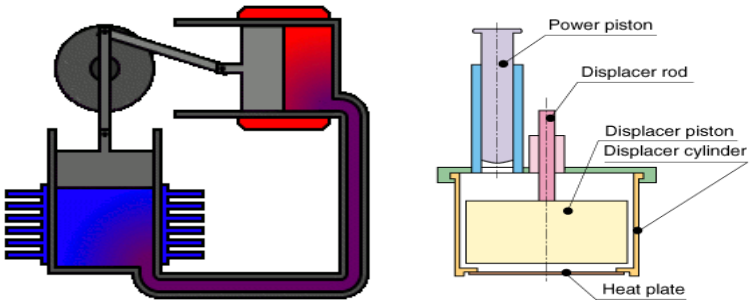

(a) (b)

Figure 1.2: Different types of Stirling engines: (a) Kinematically linked Stirling engine (Source:http://en.wikipedia.org/wiki/Stirling_engine). (b) Free Piston Stirling engine (Source: http://www.bekkoame.ne.jp/~khirata/english/fpse.htm).

and the displacer are linked so that there is a phase difference with respect to one another, and the resulting system is a single degree-of-freedom (SDOF) system. On the other hand, FPSEs are unconstrained such that the piston and the displacers move solely due to the pressure variation of the working gas caused by the temperature difference. This arrangement results in independent movement of the piston and displacer, allowing the system to be a multi-degree-of-freedom (MDOF) system, as depicted in Figure 1.2(b). A FPSE has the following advantages over the kinematic Stirling engine: (i) can be produced at a low cost, (ii) does not require external high pressure seal, (iii) long operating life without the need for lubrication, and (iv) quiet operating conditions.

The cyclic process for the movement of a kinematic Stirling engine is depicted in Figure 1.3. For a kinematic Stirling engine, initial conditions are given to the power piston to compress the working fluid in the compression space (Step 1). The working fluid is heated, increasing the pressure within the system. The heated fluid increases the pressure and pushes the power piston to its upstroke (Step 2).

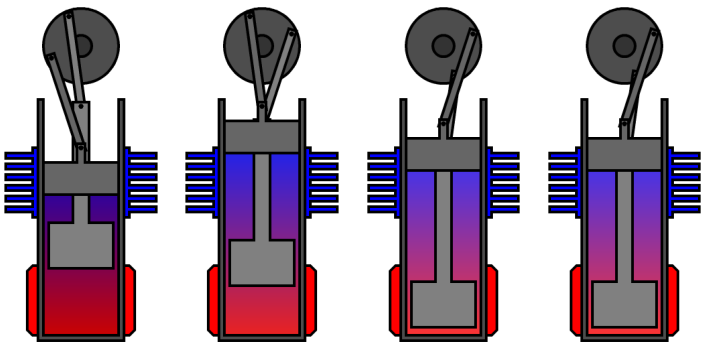

(a) Step 1 (b) Step 2 (c) Step 3 (d) Step 4

Figure 1.3: Cycles for kinematic Stirling engines (Source: http://en.wikipedia.org/wiki/Stirling_engine).

The displacer, which is kinematically linked with the power piston with a phase difference, moves the heated working fluid to the compression space (Step 3). Finally, the cooled gas is compressed by the power piston due to its momentum along with the decreased pressure (Step 4).

On the other hand, a FPSE relies on the pressure variations for its operation, as depicted in Figure 1.4. When heat is applied, the power piston of FPSE is pushed outwards by the expanding gas. The increase in volume decreases pressure in the compression space, which creates a pressure difference across the displacer. The

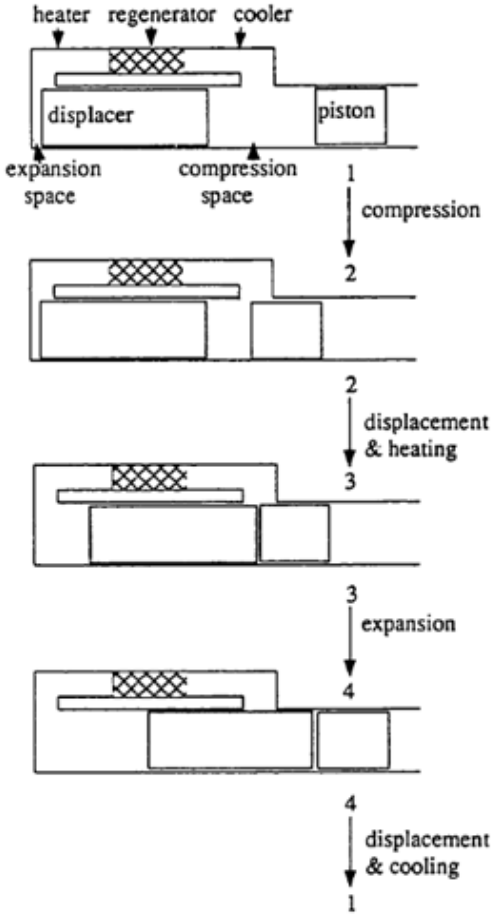

Figure 1.4: The cyclic process of free piston Stirling engines (Source: Ulusoy, 1994).

working fluid moves from the expansion space to the compression space, forcing the displacer towards the expansion space (Step 1). The power piston is almost stationary; hence, the volume within the system can be considered constant. The working gas is cooled at a constant volume, reducing the pressure of the gas. The reduced pressure causes the power piston to move towards the hot end by its own inertia, compressing the cold working fluid in the compression space (Steps 1 and 2). This increases the pressure in the compression space causes the working fluid to flow to the expansion space. This results in displacer moving towards the power piston and thus collapsing the compression space (Steps 2 and 3). As the working fluid heats up, the pressure of the system increases and causes the power piston to move outward (Steps 3 and 4), leading to a cyclic process (Walker, 1980).

Stirling engines can be further classified on the basis of their configuration as alpha, beta, and gamma type engines (Urieli and Berchowitz, 1984; Urieli, 2010). The three aforementioned configurations are illustrated in Figure 1.5. The alpha engine, shown in Figure 1.5(a), contains two pistons in two different cylinders at the opposite ends that are connected by a heater, regenerator, and cooler in series. This is the simplest type of a Stirling engine configuration but the pistons have to be sealed for proper functionality. Unlike the alpha configuration, the beta configuration, shown in Figure 1.5(b), only has one cylinder with a hot end and a cool end. The displacer sits inside the cylinder while the power piston is above the compression space. The gamma configuration, shown in Figure 1.5(c), is similar to the beta type except that the power piston and displacer are in two different cylinders. The cycles for all three configurations will depend upon whether it is a kinematic or free

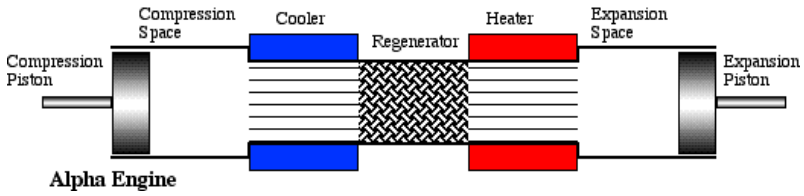

(a)

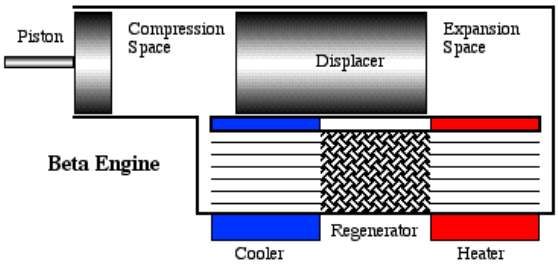

(b)

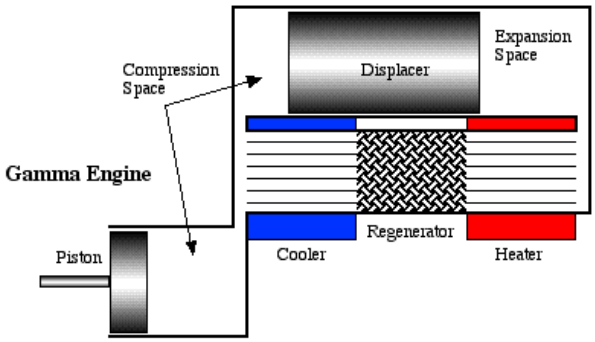

(c)

Figure 1.5: Different configurations of Stirling engines: (a) Alpha type configuration. (b) Beta type configuration. (c) Gamma type configuration (Source: Urieli, 2010).

piston Stirling engine, as described previously.

1.2 Existing Literature on FPSE Dynamics

Various studies on the FPSE are based on the Schmidt's analysis, as this approach can lead to a closed form solution for the engine performance. The Schmidt model helps relate the thermodynamics to the dynamics of the FPSE. The assumptions made in the model are as follows: (i) isothermal compression and expansion, (ii) ideal gas behavior, (iii) spatially constant pressure, and (iv) closed system en-

gine. By using the aforementioned assumptions, the working gas pressure can be determined in terms of volume variations.

In 1985, Berkowitz and Redlich did a linear analysis of FPSE using the Schmidt isothermal model to determine the requirements for oscillation and general behavior under load. The linear analysis of the system showed that the equilibrium point near the origin had one pair of complex eigenvalues with a zero or small positive real part and another pair with a negative real part. The growing oscillations need to be controlled by introducing nonlinearities to the system, such as gas springs. It is suggested to change the damping coefficients by using a control mechanism to push the positive real part of the conjugate pair towards the imaginary axis. It is also found that there is a minimum hot end temperature for which oscillations can be expected. By making the frequency of the displacer oscillations to match the frequency of the power piston oscillations, the engine can start at a lower hot end temperature and power can be maximized (Berchowitz and Redlich, 1985).

In 1990, Benvenuto, de Monte, and Farina studied a methodology for design optimization and performance evaluation of FPSE dynamics for space applications. The effects of temperature variations of the working spaces on the spring terms along with gas hysteresis losses for the buffer space and for the gas spring space are included as linear damping terms. The buffer space is the nominal space under the power piston, and the spring space is the air space that acts as a spring attached to the displacer. The developed method allows analytical relations for determining dynamic behavior for their modeled systems. The model also allows for minimizing hysteresis losses in the gas springs and viscous losses in the heat exchangers. Finally,

an analytical relationship was constructed for the phase angle between the displacer and the piston motions in order to optimize engine efficiency (Benvenuto and de Monte, 1995).

In 1994, Ulusoy investigated the nonlinear effects on FPSE through isothermal and nonisothermal modeling. The thermodynamics and dynamics of the system are coupled via isothermal and nonisothermal methods. The effects of nonlinear damper load, nonlinear pressure loss, and a gas spring acting on the displacer were studied. By using nonlinear analysis, it was shown that periodic motions of the piston and displacer can be attained and controlled by using the coefficient of the nonlinear load term. The effect of the temperature variation due to nonisothermal behavior of the working gas on FPSE was also investigated by using numerical means. The results showed that variation in the working gas temperature does not have a significant effect on the dynamics of the engine, leading to the conclusion that an isothermal assumption is appropriate for a qualitative dynamic analysis (Ulusoy, 1994).

In 2009, at the University of Maryland, in the same research group as this thesis author, Choudhary investigated how to engineer a Hopf bifurcation of an equilibrium solution in a FPSE via nonlinear analysis and simulations. Reduced-order models were developed on the basis of Schmidt and nodal analysis. Through eigenvalue analysis, it was shown that introducing an appropriate nonlinearity into the system can lead to a Hopf bifurcation, the result of which can be an attracting limit cycle. The method of multiple scales was used to study the weakly nonlinear system analytically in order to develop limit-cycle motions in a beta FPSE with cubic damping on the power piston side. The analytical prediction was compared to

numerical results, which show that the analytical and numerical solutions are close to one another near the bifurcation point. Finally, a simplified nodal method was developed to reduce the order of FPSE model that captures more of the thermodynamic behavior than the Schmidt model, while making the analysis of the dynamics possible. However, the simplified nodal methods presented in the thesis study did not yield physically valid models (Choudhary, 2009). This thesis builds upon the studies conducted by Choudhary. Here, further parametric tests are conducted to evaluate various parameters that can introduce Hopf instabilities. Additional nonlinearities that can produce oscillatory motions are introduced into the system and studied. Finally, experimental studies are done.

1.3 Contributions

A main purpose of this study is to better understand oscillatory motions in a FPSE by introducing nonlinearities into the system. A FPSE system with gas spring for the displacer and a nonlinear spring for the power piston are introduced. The introduction of the spring parameters gives one the ability to change the design frequency of the FPSE without much trouble when the masses of the pistons are constrained. This system is linearized to observe which parameters, in particular, the spring parameter and the damping parameter, affect the Hopf instabilities. Through root locus analysis, the influences of the stiffness of the system and the damping are assessed. Next, the effect of cubic nonlinear spring addition to the power piston is studied through numerical studies to see if limit-cycle motions can be attained.

This finding can be applied to FPSEs without cubic damping in order to introduce limit-cycle motions. Once this was completed, magnetic springs are introduced in the displacer and power pistons to study if the FPSE system can exhibit limit-cycle motions. A study of the effects of the magnetic springs on the FPSE is carried out to see if this is a viable option for application. After the magnetic spring model showed an oscillatory motion, an experimental setup is fabricated and the motions of the displacer and piston are studied. A recent study conducted on FPSEs is the study of Formosa (2009).

1.4 Thesis Organization

In the next chapter, the governing equations are presented. First, the Schmidt analysis is provided and the general form of the FPSE governing equations is givem. Second, a spring parameter is introduced into the gas spring FPSE studied by Ulusoy (Ulusoy, 1994). The pressure losses within the FPSE are also derived. In Chapter 3, a parametric study is presented for the various cases of the modified gas spring FPSE. Afterwards, the governing equations for the magnetic spring system are derived in Chapter 4 and numerical studies carried out for the magnetic spring FPSE are presented. The fabrication details and experimental studies for the FPSE are presented in Chapter 5. Summary and future work are provided in Chapter 6 along with concluding remarks. To close this thesis, in the appendices, some details of Ulusoy's work , the experimental parameters, and the codes used in the work are provided.

Chapter 2

Governing Equations

The governing equations of motions for the displacer and power piston are obtained by using force balance for a beta type FPSE. However, this methodology can be used for any other type of FPSE as well. By using Schmidt analysis, the thermodynamics of the system is described as algebraic functions of the displacements and velocities of the displacer and power piston. Subsequently, a nonlinear spring term is added to the power piston of the gas spring FPSE studied by Ulusoy (Ulusoy, 1994). The equations of motion for the modified case are provided along with the parameters used in the studies carried out in Chapter 3. The pressure loss for a general type of FPSE is also derived in this chapter.

2.1 Dynamic Equations

The dynamic equations for the schematic of FPSE configuration shown in Figure 2.1 are derived. The FPSE can be considered as a two DOF system governed by force balance of pressure, spring, and external load forces. The net force acting on the displacer piston and the power piston is a resultant of the pressure difference between the two sides of the pistons. Hence, applying Newton's second law, the

equations of motion for the given FPSE can be written as:

$$m_d\ddot{x}_d = A_d(P_c - P_e) - F_{spring_1} \tag{2.1}$$

$$m_p\ddot{x}_p = A_p(P_b - P_c) + F_{load}\dot{x}_p - F_{spring_2} \tag{2.2}$$

where A_d is the area of the displacer, A_p is the area of the piston, m_d is the mass of the displacer, m_p is the mass of the piston, V_b is the nominal volume under the power piston, P_b is the nominal pressure under the power piston, and F_{load} is an external load that is attached to the power piston. The numerical values given for

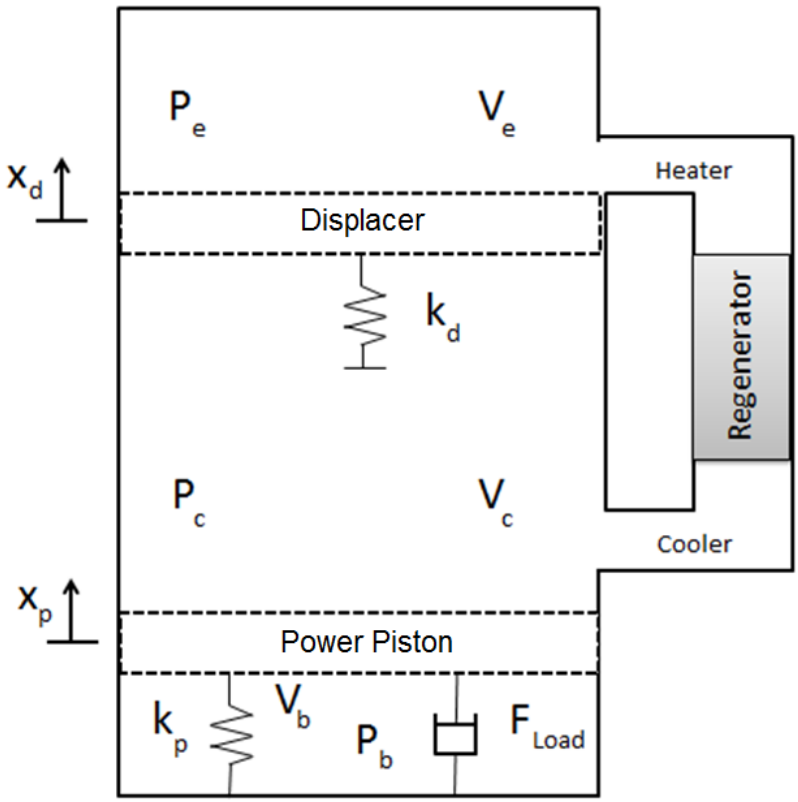

Figure 2.1: Schematic of a beta type FPSE.

F_{load} should be negative because since this load parameter represents energy being taken out of the system by equipment such as an alternator.

To solve equations (2.1) and (2.2), one requires information about the pressures in the expansion, compression, and buffer space. The working gas pressure is dependent on the displacements of the piston and the displacer. In the following section, pressure is related to the volume via Schmidt analysis.

2.2 Schmidt Analysis

In 1871, an isothermal analysis of the Stirling engine was completed by Gustav Schmidt. Major assumptions of this analysis are isothermal compression and expansion, perfect regeneration, and spatially constant instantaneous working gas pressure. The Schmidt analysis provides a simple way to relate the dynamics and thermodynamics of the system.

The pressure terms are modeled as a function of the volume and the temperature. For this, the conservation of mass and the ideal gas law are used. By using the conservation of mass, the total mass of working gas inside the engine can be expressed as (Urieli and Berchowitz, 1984)

$$m_t = m_e + m_h + m_R + m_k + m_c \tag{2.3}$$

where m_t is the total mass of the working gas, m_e is the mass of the gas inside the expansion space, m_h is the mass of the gas inside the heater, m_R is the mass of the gas inside the regenerator, m_k is the mass of the gas inside the cooler, and m_c is the

mass of the gas in the compression space.

An assumption of instantaneous working gas pressure is made, which leads to

$$P \approx P_e \approx P_h \approx P_R \approx P_k \approx P_c \tag{2.4}$$

It is also assumed that the temperature of expansion space is equal to the heater temperature and the temperature of the compression space is equal to the cooler temperature:

$$T_e = T_h \; and \; T_c = T_k \tag{2.5}$$

Hence,using the ideal gas relation: $m_t = \sum \frac{PV}{RT}$, the total mass of the working gas can be written as

$$m_t = \frac{P}{R}\left[\frac{V_e}{T_h} + \frac{V_h}{T_h} + \frac{V_R}{T_R} + \frac{V_k}{T_k} + \frac{V_c}{T_k}\right] \tag{2.6}$$

where V_e, V_h, V_R, V_k, and V_c are the respective volumes. The temperature along the regenerator is assumed to be linear as shown in Figure 2.2. Hence, the temperature

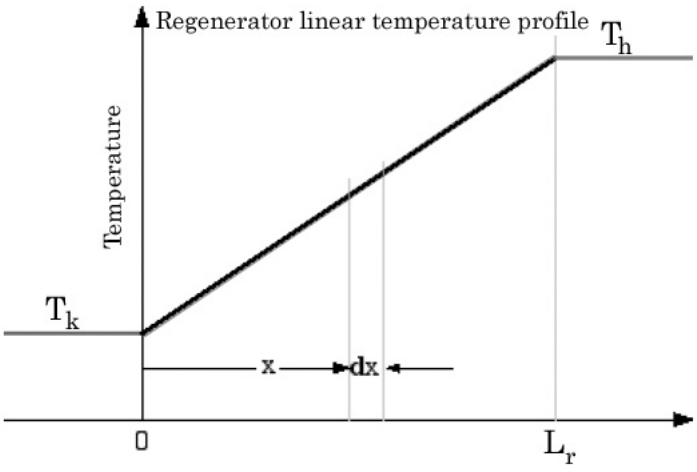

Figure 2.2: Assumed temperature profile of regenerator (Source: Urieli, 2010).

in the regenerator can be extrapolated as

$$T(x) = \frac{(T_h - T_k)x}{L_r} + T_k \tag{2.7}$$

where L_r is the regenerator length. Now, the total mass of the gas in the regenerator can be found by using ideal gas relationship:

$$m_r = \frac{V_r P}{R} \int_0^{L_r} \frac{dx}{(T_h - T_k)x + T_k L_r} \tag{2.8}$$

$$m_r = \frac{V_r P}{R} \frac{ln(T_h/T_k)}{(T_h - T_k)} \tag{2.9}$$

Hence, the regenerator temperature is found to be

$$T_R = \frac{T_h - T_k}{\ln (T_h/T_k)} \tag{2.10}$$

Next, the compression volume and expansion volume is defined by the geometry of the system; that is,

$$V_c = V_{cm} - A_p x_p + A_d x_d \tag{2.11}$$

$$V_e = V_{em} - A_d x_d \tag{2.12}$$

where V_{cm} is the mean compression volume and V_{em} is the mean expansion volume.

Next, new parameters are introduced for the simplification:

$$S = \frac{V_{em}}{T_h} + \frac{V_h}{T_h} + \frac{V_R \ln\left(\frac{T_h}{T_k}\right)}{T_h - T_k} + \frac{V_k}{T_k} + \frac{V_{cm}}{T_k} \tag{2.13}$$

$$a = \frac{A_p}{T_k}\frac{1}{S} \tag{2.14}$$

$$b = \left[\frac{A_d}{T_k} - \frac{A_d}{T_h}\right]\frac{1}{S} \tag{2.15}$$

On substituting equations (2.10), (2.11), and (2.12) into equation (2.6) and using equations (2.13), (2.14), and (2.15), the pressure term can be determined as

$$P = \frac{m_t R}{S\left(1 - ax_p + bx_d\right)} \tag{2.16}$$

It is assumed that the pressure of the working gas is equal to the mean pressure, $P = P_m$, when the displacer and the piston are at mid-stroke; that is $x_p = 0$ and $x_d = 0$. Hence, the mean pressure can be expressed as

$$P_m = \frac{m_t R}{S} \tag{2.17}$$

By using equation (2.17), the working space pressure can be expressed as

$$P = \frac{P_m}{1 - ax_p + bx_d} \tag{2.18}$$

It is assumed that the compression pressure is equal to the working gas pressure, and the expansion pressure is the compression pressure minus pressure drop (ΔP)

across the heater, regenerator, and cooler. It is also assumed that the buffer pressure is equal to the mean pressure (Ulusoy, 1994).

$$P_c = P \tag{2.19}$$

$$P_e = P_c - \Delta P \tag{2.20}$$

$$P_b = P_m \tag{2.21}$$

Hence, the equations of motions become

$$m_d \ddot{x}_d = A_d \Delta P - F_{spring_1} \tag{2.22}$$

$$m_p \ddot{x}_p = A_p P_m \left(1 - \frac{1}{F}\right) + F_{load} \dot{x}_p - F_{spring_2} \tag{2.23}$$

$$F = 1 - a x_p + b x_d \tag{2.24}$$

2.3 System with Gas Spring

In 1994, Ulusoy studied the effects of nonlinearity in a FPSE. One such study was the modeling of gas spring to introduce nonlinearity into the system, as shown in Figure 2.3. In this section, the equations of motions are presented after adding a spring parameter to the power piston of the gas spring FPSE studied by Ulusoy.

The gas spring is modeled by assuming ideal gas relation for an adiabatic

process and defining the gas spring volume (Ulusoy, 1994)

$$P_s = P_m \left(\frac{V_{sm}}{V_s} \right)^{\gamma} \tag{2.25}$$

$$V_s = V_{sm} + A_r x_d \tag{2.26}$$

where V_s is the gas spring volume, V_{sm} is its average value, and A_r is the area of the gas spring rod. Introducing a new quantity

$$c = \frac{A_r}{V_{sm}} \tag{2.27}$$

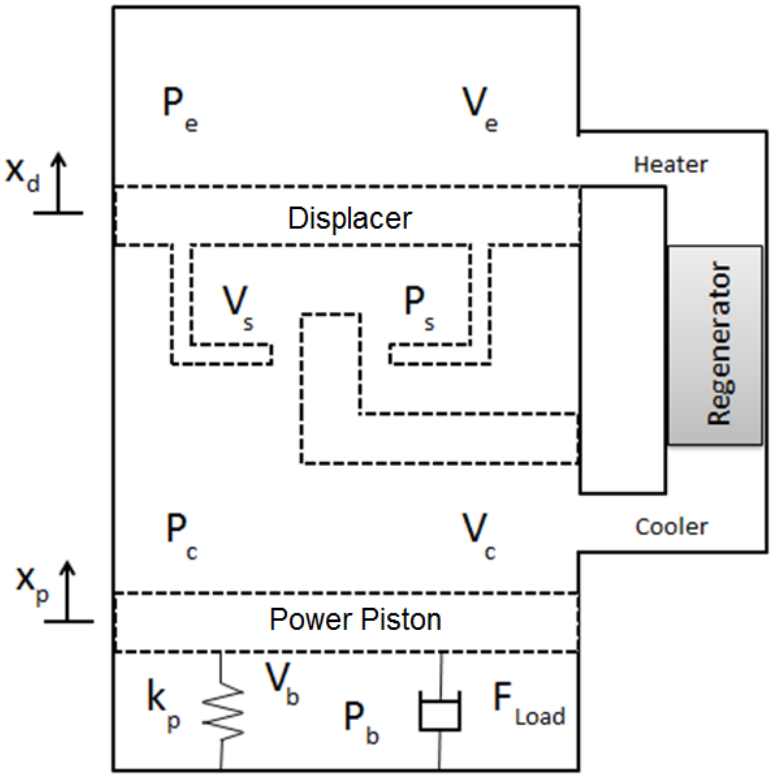

Figure 2.3: Schematic of a gas spring beta type FPSE.

the gas spring pressure term can be written as:

$$P_s = P_m \left(\frac{1}{1 + cx_d} \right)^{\gamma} \tag{2.28}$$

Also, the b parameter in equation (2.24) should have the area of gas spring rod (A_r) taken into account as well. This means

$$b = \left[\frac{A_d - A_r}{T_k} - \frac{A_d}{T_h} \right] \frac{1}{S} \tag{2.29}$$

After the spring parameter is added to the power piston as shown in Figure 2.3, the equations of motion for the gas spring FPSE become

$$m_d \ddot{x}_d = A_d \left(P_c - P_e \right) - A_r \left(P_c - P_s \right) \tag{2.30}$$

$$m_p \ddot{x}_p = A_p \left(P_b - P_c \right) + F_{load} \dot{x}_p - F_{spring} \tag{2.31}$$

2.4 Pressure Loss Term

The pressure drop term, ΔP, can be expressed as

$$\Delta P = \Delta p_{cooler} + \Delta p_{regenerator} + \Delta p_{heater} \tag{2.32}$$

In this thesis study, including the experimental setup, the FPSE does not include a regenerator; hence, the pressure loss in the regenerator is ignored. Without the regenerator, the pressure drop can be modeled as a continuous pressure drop through

one channel assuming the geometry of the channel does not vary. Thus, the pressure drop is modeled only as a drop through the cooler area. It is assumed that the working fluid acts turbulently inside the FPSE. Hence, the pressure drop derived by Urieli is used (Urieli and Berchowitz, 1984)

$$\Delta P_{cooler} = \frac{1}{2}\rho\left(f_t + k_h\right) u_{cooler}|u_{cooler}| \tag{2.33}$$

where ρ is the density of the working fluid, k_h is the head loss, u is the velocity of the working fluid, and f_t is the turbulent friction. This factor is given by

$$f_t = \frac{4 f_f L}{d_h} \tag{2.34}$$

where f_f is the Fanning friction coefficient factor, L is the length of the flow passage, and d_h is the hydraulic diameter. The Fanning friction coefficient factor is defined as

$$f_f = C_f Re^n \tag{2.35}$$

where Re is the Reynolds number defined as

$$Re = \frac{\rho U d_h}{\mu} \tag{2.36}$$

and μ is the viscosity of the working fluid. Some commonly used working gases' viscosities can be calculated by using relations given by Martini (1983). The recommended values for C_f and n depend on the details of the flow.

Next, the gas flow velocities need to be related to those of the reciprocating elements. This is done by defining the volumetric flow rate of the compression and expansion space through

$$\dot{V}_c = \frac{dV_c}{dt} \tag{2.37}$$

$$\dot{V}_e = \frac{dV_e}{dt} \tag{2.38}$$

Taking the respective term derivatives of equations (2.10) and (2.11), the following relationships are found:

$$\dot{V}_c = A_d\dot{x}_d - A_p\dot{x}_p \tag{2.39}$$

$$\dot{V}_e = -A_d\dot{x}_d \tag{2.40}$$

Next, the velocity of gas with respect to the velocities of the pistons are approximated as

$$u_{cooler} = \frac{\dot{V}}{A_{cooler}} \tag{2.41}$$

where $\dot{V} = \dot{V}_e - \dot{V}_c$ because positive values of $\dot{V}_e$ and $\dot{V}_c$ indicate increasing volumes, which results in

$$\dot{V} = A_p\dot{x}_p - 2A_d\dot{x}_d \tag{2.42}$$

Finally, inserting equation (2.42) into equation (2.41), and then into equation (2.32), the pressure drop can be written as

$$\Delta P = \frac{1}{2}\rho\left(f_t + k_h\right)\left[\frac{A_p\dot{x}_p - 2A_d\dot{x}_d}{A_k}\left|\frac{A_p\dot{x}_p - 2A_d\dot{x}_d}{A_k}\right|\right] \tag{2.43}$$

Chapter 3

Parametric Studies

In this chapter, parametric studis are pursued by using the model presented in the previous chapter. This model is shown in Figure 3.1. The numerical studies help understand which parameters push the Stirling engine to exhibit Hopf instabilities. The equations of motions reported in Ulusoy's study are given in Appendix A. In that study, the equations of motion are rewritten by first nondimensionalizing the

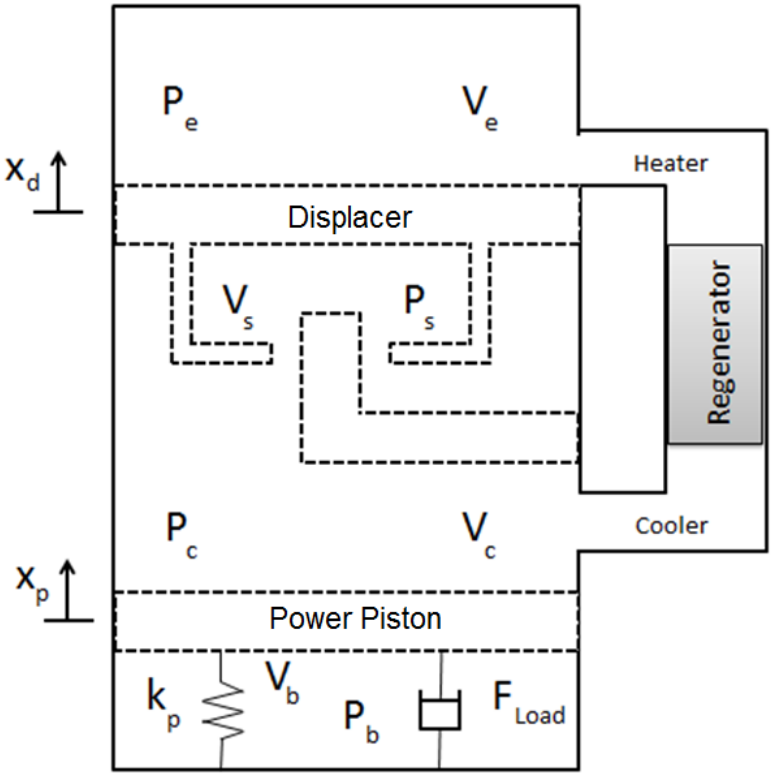

Figure 3.1: Schematic of a gas spring beta type FPSE.

equations and then expanding the nonlinear terms by using Taylor series. Also, the pressure loss terms are separated as a combination of linear and nonlinear terms (Ulusoy, 1994). For the purposes of this study, a spring parameter is introduced into the power piston to study Hopf instabilities. The significance of the new spring parameter becomes apparent for FPSEs without cubic damper, as this nonlinearity can help realize oscillatory motions. Additionally, one can change the oscillation frequency of the system through the spring parameter. The frequency response of the system is determined by the displacer and piston masses. However, in practice, these parameters cannot be easily changed. On the other hand, one can easily change the frequency of the sytem through springs to get a desired frequency associated with a periodic motion..

The equations of motions of the modified syste have been reported in Chapter 2.3 and are presented in equations (2.30) and (2.31). Next, the equations are put in state-space form for the system with the gas spring:

$$\dot{x} = \begin{bmatrix} 0 & 1 & 0 & 0 \\ k_1 & c_1 & k_2 & c_2 \\ 0 & 0 & 0 & 1 \\ k_3 & 0 & k_4 - \dfrac{\tilde{k}_p}{\tilde{m}_p} & \dfrac{\tilde{f}_l}{\tilde{m}_p} \end{bmatrix} \begin{bmatrix} x_1 \\ x_2 \\ x_3 \\ x_4 \end{bmatrix} + \begin{bmatrix} 0 \\ \epsilon_1 HOT_1 + \epsilon_2 HOT_2 \\ 0 \\ -\dfrac{\tilde{f}_c}{\tilde{m}_p} x_3^2 x_4 + \epsilon_3 HOT_3 \end{bmatrix} \tag{3.1}$$

Here,

$$\tilde{x}_d = x_1 \tag{3.2}$$

$$\dot{\tilde{x}}_d = x_2 \tag{3.3}$$

$$\tilde{x}_p = x_3 \tag{3.4}$$

$$\dot{\tilde{x}}_p = x_4 \tag{3.5}$$

$$\tilde{k}_p = \frac{l_p k_p}{2A_p P_m} \tag{3.6}$$

$$\tilde{f}_l = \frac{F_{load}}{A_p P_m} \tag{3.7}$$

For the parametric studies, the parameters given by Ulusoy are used. The pressure loss model is given by (Ulusoy, 1994)

$$\Delta P = -0.028x_2 - 0.511x_2^3 + 0.021x_4 + 1.197x_2^2x_4 - 0.979x_2x_4^2 + 0.269x_4^3$$

Finally, the derived state-space model is given by

$$\dot{x} = \begin{bmatrix} 0.00 & 1.00 & 0.00 & 0.00 \\ -0.38 & -1.60 & -1.30 & 1.20 \\ 0.00 & 0.00 & 0.00 & 1.00 \\ 0.62 & 0.00 & -1.06 - \dfrac{\tilde{k}_p}{0.26} & \dfrac{\tilde{f}_l}{0.26} \end{bmatrix} \begin{bmatrix} x_1 \\ x_2 \\ x_3 \\ x_4 \end{bmatrix} + \begin{bmatrix} 0 \\ \epsilon_1 HOT_1 + \epsilon_2 HOT_2 \\ 0 \\ -\dfrac{\tilde{f}_c}{0.26}x_3^2x_4 + \epsilon_3 HOT_3 \end{bmatrix} \tag{3.8}$$

where

$$HOT_1 = -26.21x_2^3 + 66.38x_2^2x_4 - 53.21x_2x_4^2 + 15.31x_4^3$$

$$HOT_2 = 0.002x_1^2 - 0.001x_1^3 - 0.007x_1x_3 - 0.002x_1^2x_3 - 0.006x_3^2 - 0.003x_1x_3^2 - 0.002x_3^3$$

$$HOT_3 = 0.025x_1^2 - 0.004x_1^3 - 0.085x_1x_3 - 0.02x_1^2x_3 - 0.074x_3^2 - 0.035x_1x_3^2 - 0.02x_3^3$$

3.1 Parametric Investigations using Root Locus Plots

The system of equations is solved for the equilibrium points, which is found to be at the origin (0.00,0.00,0.00,0.00). In order to study the behavior of the system, the Jacobian of the system at the equilibrium point is investigated:

$$[D_i f] = \begin{bmatrix} 0.00 & 1.00 & 0.00 & 0.00 \\ -0.38 & -1.60 & -1.30 & 1.20 \\ 0.00 & 0.00 & 0.00 & 1.00 \\ 0.62 & 0.00 & -1.06 - \dfrac{\tilde{k}_p}{0.26} & \dfrac{\tilde{f}_l}{0.26} \end{bmatrix} \tag{3.9}$$

The characteristic equation is derived from the Jacobian and used to study the instabilities of the system are studied. A parametric study is done by varying $\tilde{k}_p$, the stiffness of spring, and $\tilde{f}_l$, the linear damping parameter associated with power piston. The goal is to realize a system that exhibits limit-cycles through a Hopf bifurcation. The criteria for a Hopf bifurcation of an equilibrium point are given by (Nayfeh and Balachandran, 1995)

i) The system has an equilibrium point $x = x_0$ at the critical point $\alpha = \alpha_c$.

ii) The Jacobian has a pair of purely imaginary eigenvalues while all of the other eigenvalues have non-zero real parts at (x_0, α_c).

iii) For $\alpha \cong \alpha_c$, let the analytic continuation of the pair of imaginary eigenvalues be $\lambda \pm i\omega$. Then $\dfrac{d\lambda}{d\alpha} \neq 0$ at $\alpha \cong \alpha_c$.

In this thesis work, the parameters $\tilde{f}_l$ and $\tilde{k}_p$ are synonymous with the two parameter. Condition (i) is met by solving for the equilibrium point. After using the approximate values of -0.10 and 0.10 for $\tilde{f}_l$ and $\tilde{k}_p$, respectively. It is found that the system is "close" to satysfying the Condition (ii); the associated eigenvalues of the Jacobian matrix are

$$\lambda_{1,2} = -0.99 \pm 0.76i$$

$$\lambda_{3,4} = \pm 0.94i$$

Condition (iii) requires the eigenvalues to cross the imaginary axis with nonzero speed, called the transversality condition. When the eigenvalues cross the imaginary axis, then, there must be a point when the Jacobian matrix has a pair of purely imaginary eigenvalues. In order to check the transversality condition, the root locus plots of the system are observed as the parameters $\tilde{k}_p$ and $\tilde{f}_l$ are varied. First, the value of the spring parameter, $\tilde{k}_p$, is set to zero and the value of the linear load parameter, $\tilde{f}_l$, is varied. Next, $\tilde{f}_l$ is set to zero and $\tilde{k}_p$ is varied. Finally, both $\tilde{k}_p$ and $\tilde{f}_l$ are varied to observe how the root locus plots change. Through the numerical studies, one can examine which parameters are important and can be tuned to introduce Hopf instabilities.

Since it can be assumed that the load is dissipating energy from the system, the linear load parameter ($\tilde{f}_l$) is varied from -1.00 to 0.00 and spring term is set to

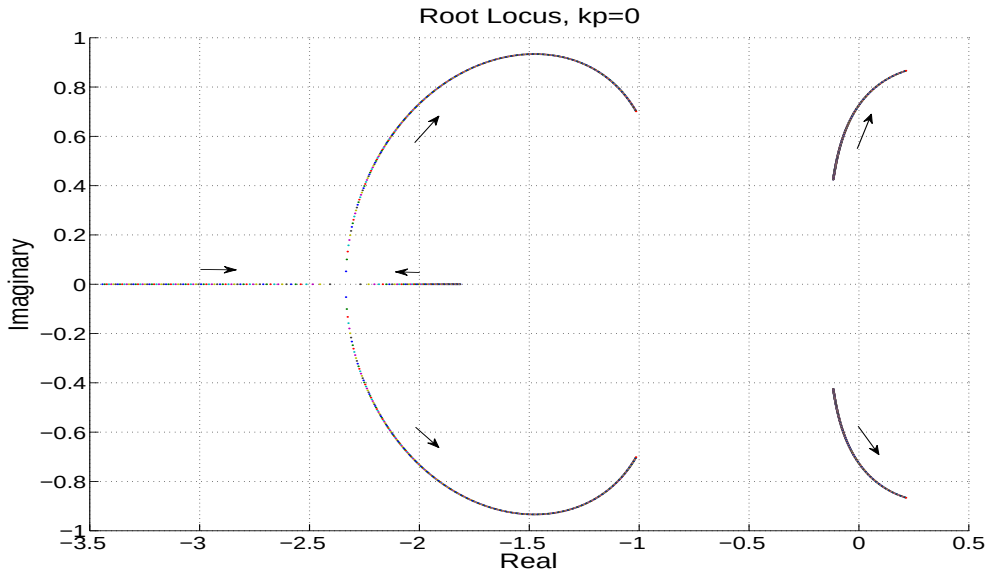

Figure 3.2: Root locus plot with spring parameter, $\tilde{k}_p$, set to zero while linear load parameter, $\tilde{f}_l$, is varied from -1.00 to 0.00.

0.00 for generating the plot shown in Figure 3.2. The values of $\tilde{f}_l$ are only varied upto 0.00 since positive values would mean that energy is being added to the system. It can be seen that one pair of the eigenvalues crosses the imaginary axis, whereas the other pair has a negative real part. The system has only one pair of eigenvalues that becomes purely imaginary whereas the second pair has real and imaginary parts, which meets the Hopf instability condition (ii). It can also be seen from the graph that the transversality condition for a Hopf instability is met. The value for $\tilde{f}_l$ at which there is a pair of purely imaginary eigenvalues is approximately -0.22, which is the same as what Ulusoy (1994) had determined. This is expected since when $\tilde{k}_p$ is 0.00, both systems are identical.

Next, the spring parameter is varied from 1.00 to 0.00, while the linear load parameter is set to 0.00, as shown in Figure 3.3. It can be seen that a pair of eigenvalues cross the imaginary axis while the other pair has a negative real part.

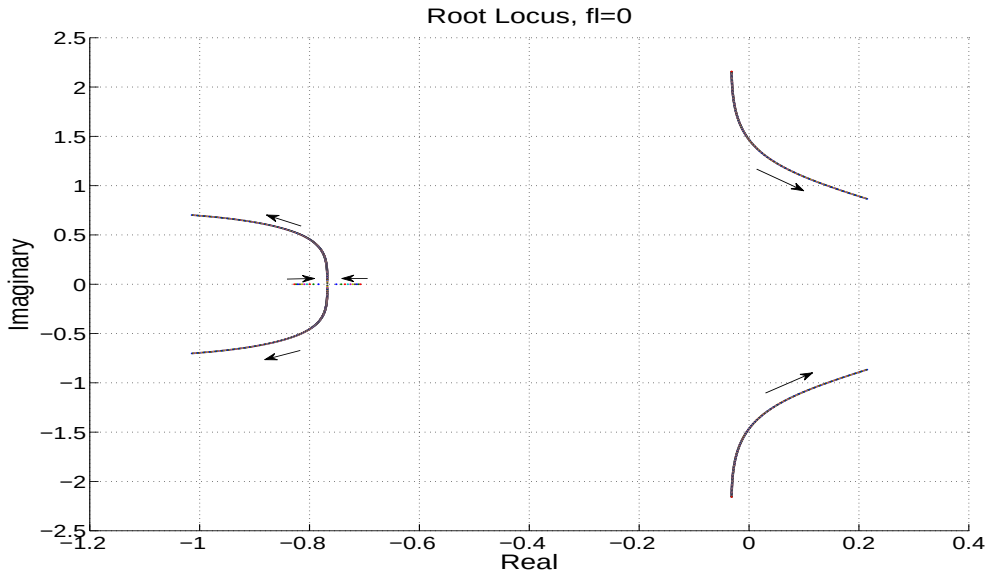

Figure 3.3: Root locus plot with linear load parameter, $\tilde{f}_l$, set to zero while spring parameter, $\tilde{k}_p$, is varied from 1.00 to 0.00.

Like the first case, this case meets both the Hopf instability conditions (ii) and (iii). The value of $\tilde{k}_p$ at which there is a pair of purely imaginary eigenvalues is approximately 0.40.

Finally, both $\tilde{f}_l$ is varied for various values of $\tilde{k}_p$ to determine their combined effect on the system. From Figure 3.4, it can be seen that as $\tilde{k}_p$ increases, the conditions for a Hopf instability are not met. As the stiffness increases, the linear load parameter needs to decrease in order to meet the Hopf instability criteria. The value found by Ulusoy (1994) for $\tilde{f}_l$ without any spring parameter was -0.22, whereas when the spring parameter with value of 0.10 is added, the value for $\tilde{f}_l$ has to be approximately -0.10 in order to meet the criterion for Hopf instability. Beyond a certain linear spring parameter value, one pair of eigenvalues does not cross the imaginary axis. This observation points to the important role played by the stiffness parameter in determining Hopf instabilities.

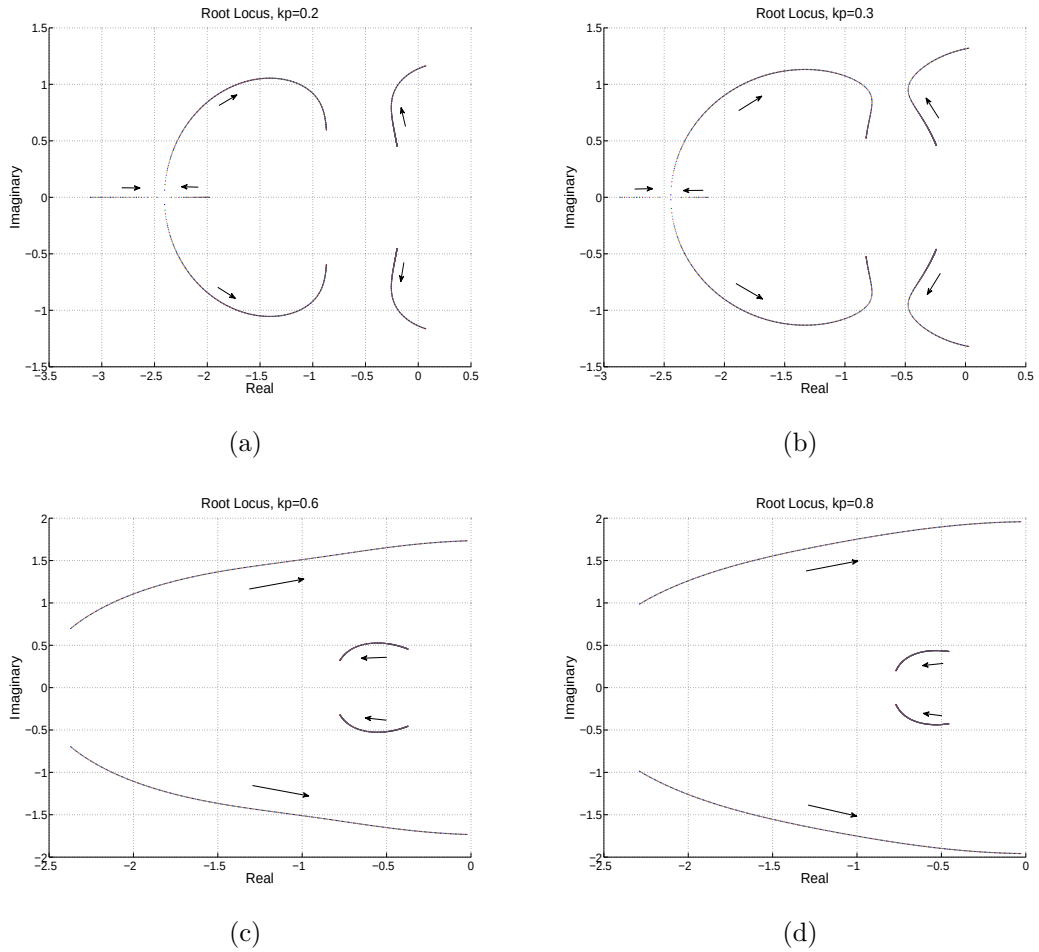

Figure 3.4: Root Locus Plot with varying $\tilde{f}_l$ and $\tilde{k}_p$. (a) $\tilde{f}_l$: -1.00 to 0.00 and $\tilde{k}_p$=0.20. (b) $\tilde{f}_l$: -1.00 to 0.00 and $\tilde{k}_p$=0.30. (c) $\tilde{f}_l$: -1.00 to 0.00 and $\tilde{k}_p$=0.60. (d) $\tilde{f}_l$: -1.00 to 0.00 and $\tilde{k}_p$=0.80.

3.2 Effect of Nonlinear Spring

The stability of periodic solutions in the presence of nonlinear pressure loss and nonlinear damping load terms have been studied by Ulusoy (1994). He concluded that the nonlinear pressure loss and the nonlinear damping load terms both help produce limit-cycle motions. Here, the efforts are focused on studying the effect of the nonlinear spring term added to the power piston. For a nonlinear spring function, a series expansion of the function can be written as a combination of

linear and nonlinear spring components. In this study, a nonlinear spring with a linear spring element and a cubic nonlinear spring element is chosen. The force-displacement relationship is described as

$$F(x) = kx + \alpha k x^3 \tag{3.10}$$

where α is the nonlinear spring coefficient. A positive value of α results in a hardening spring while a negative value of α results in a softening spring (Balachandran and Magrab, 2003). The use of softening spring can cause the system equilibrium position to be unstable; hence, a hardening spring is used in this study. The state-space model for the system is

$$\dot{x} = \begin{bmatrix} 0.00 & 1.00 & 0.00 & 0.00 \\ -0.38 & -1.60 & -1.30 & 1.20 \\ 0.00 & 0.00 & 0.00 & 1.00 \\ 0.62 & 0.00 & -1.06 - \dfrac{\tilde{k}_p}{0.26} & \dfrac{\tilde{f}_l}{0.26} \end{bmatrix} \begin{bmatrix} x_1 \\ x_2 \\ x_3 \\ x_4 \end{bmatrix} + \begin{bmatrix} 0 \\ \epsilon_1 HOT_1 + \epsilon_2 HOT_2 \\ 0 \\ -\dfrac{\tilde{f}_c}{0.26} x_3^2 x_4 + \epsilon_3 HOT_3 - \tilde{k}_c x_3^3 \end{bmatrix} \tag{3.11}$$

With the linear spring parameter value, $\tilde{k}_p$, of 0.10 and the linear load term set to 0.00, the system is expected to be unstable when all the nonlinearities are excluded. The expected outcome is verified in Figure 3.5, with initial displacements for displacer and power piston set at a value of 1.00 unit, while the velocities are set to 0.00 units; the initial conditions (ICs) are presented as (x_d $\dot{x}_d$ x_p $\dot{x}_p$). The

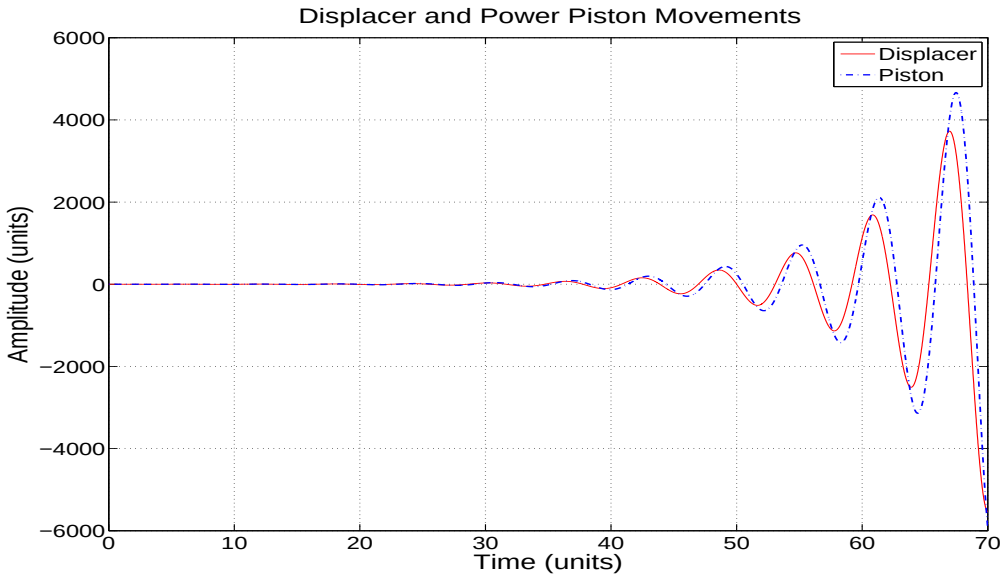

Figure 3.5: Displacement response of the displacer and the power piston excluding nonlinear terms. The chosen parameters are $\tilde{f}_l = 0.00$ and $\tilde{k}_p = 0.10$.

eigenvalues for the linearized system are given by

$$\lambda_{1,2} = 0.14 \pm 1.01i$$

$$\lambda_{3,4} = -0.94 \pm 0.66i$$

where the eigenvalues $\lambda_{1,2}$ dominate; the associated oscillation frequency is approximately 1 rad/s. Next, both the linear spring parameter, $\tilde{k}_p$, and the linear damping parameter, $\tilde{f}_l$ are set to 0.10. The system response is still unstable with the linear damping term, as shown in Figure 3.6.

Next, all of the nonlinear terms shown in equation (3.11) except the cubic spring term are held fixed at 0.00. The values of $\tilde{k}_p = 0.10$, $\tilde{k}_c = 0.10$, and $\tilde{f}_l = 0.00$ are chosen to determine the effect of nonlinear spring added to the power piston. The

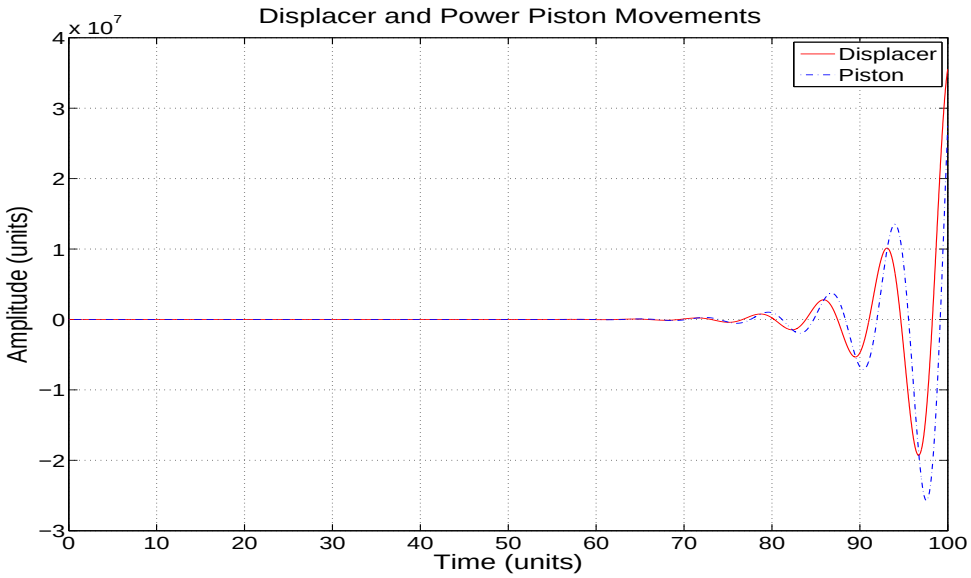

Figure 3.6: Displacement response of the displacer and the power piston excluding nonlinear terms. The chosen parameters are $\tilde{f}_l = 0.10$ and $\tilde{k}_p = 0.10$.

initial condition to generate Figure 3.7(a) is (1.00 0.00 1.00 0.00), while the initial condition for Figure 3.7(b) is (7.00 0.00 7.00 0.00). The results are presented in terms of nondimensional values, represented by units. Comparing Figure 3.7(a) and Figure 3.7(b), the amplitude for the oscillating motions for different intial conditions are about the same: about 3.89 units for the power piston, and 2.82 units for the displacer. This is further analyzed through phase portraits as illustrated in Figure 3.8, for the two different initial conditions. Figure 3.8(a) is the phase portrait for the displacer piston and Figure 3.8(b) is the phase portrait for the power piston. It can be seen that by adding a cubic spring term to power piston, the result is a limit-cycle motion when all of the other nonlinearities are not included.

Next, the cubic spring system is compared to the system studied by Ulusoy (1994). The nonlinear pressure loss terms and nonlinear gas spring terms are included in the cubic spring system ($\epsilon_1 = 1$, $\epsilon_2 = 1$, and $\epsilon_3 = 1$ in equation (3.11)).

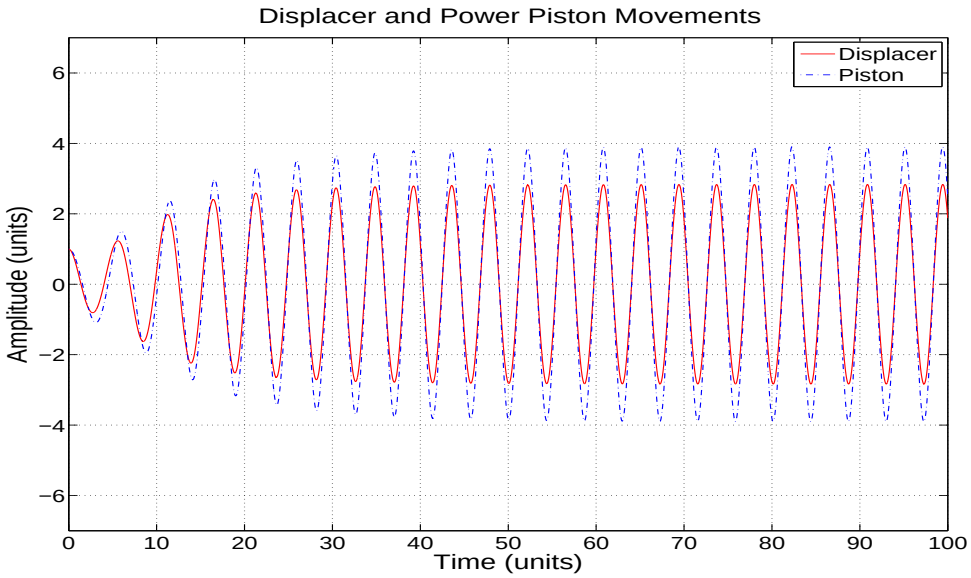

(a)

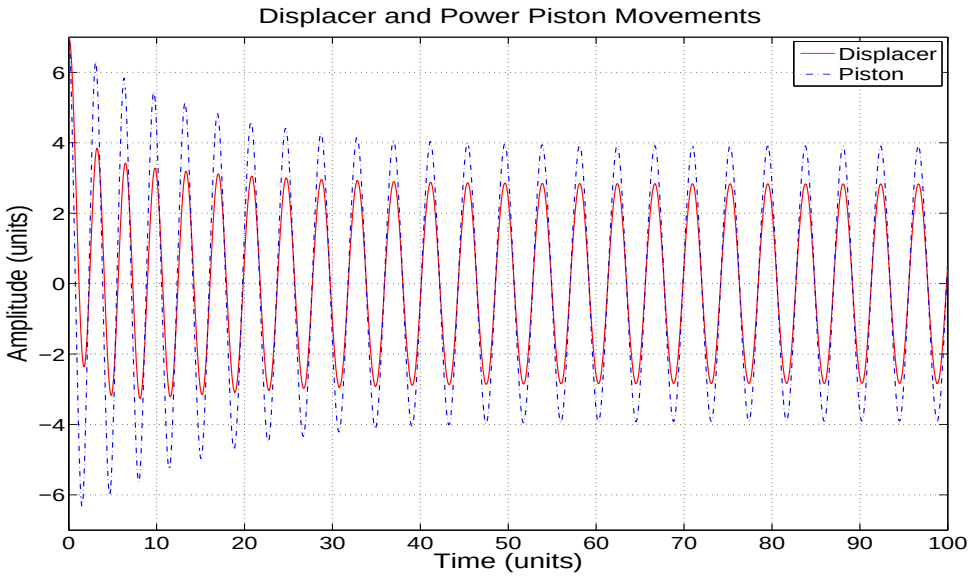

(b)

Figure 3.7: Displacement responses for the displacer and the power piston due to additional nonlinear spring added to the power piston. The parameters are $\tilde{k}_p = 0.10$, $\tilde{k}_c = 0.10$, and $\tilde{f}_l = 0.00$. (a) ICs: (1.00 0.00 1.00 0.00) and (b) ICs: (7.00 0.00 7.00 0.00).

Reasonable values for $\tilde{k}_p$ and $\tilde{k}_c$ also must be chosen. By using the parameters given by Ulusoy (1994) and substituting them into the nondimensional form of spring

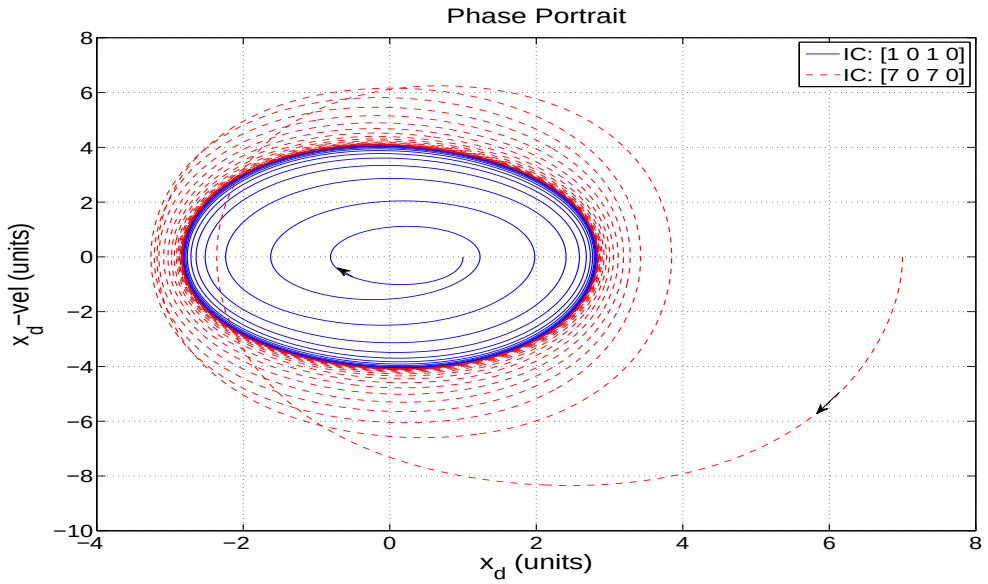

(a)

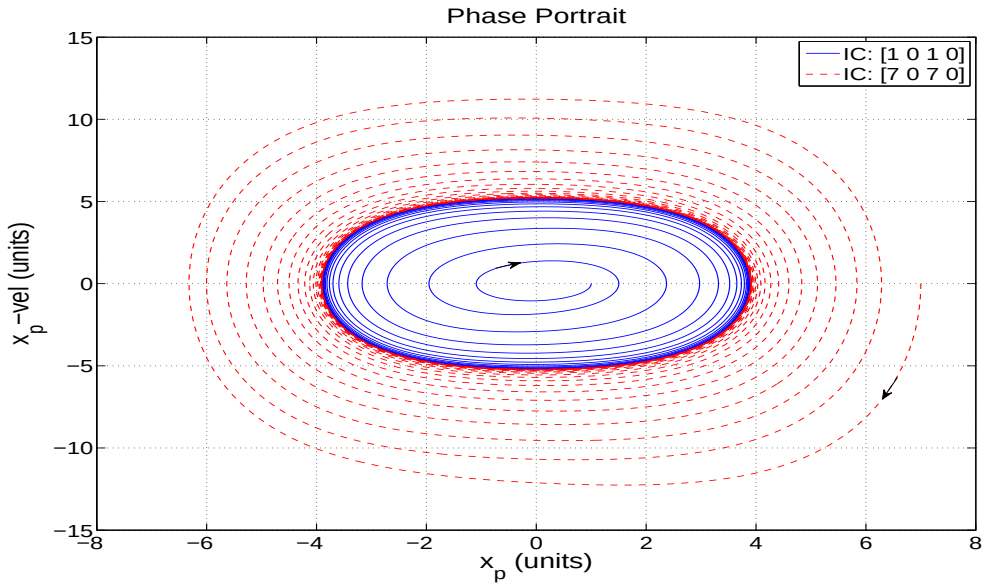

(b)

Figure 3.8: Phase portraits with chosen initial conditions of (1.00 0.00 1.00 0.00) and (7.00 0.00 7.00 0.00). (a) Response of displacer and (b) Response of power piston.

parameters, $\tilde{k}_p$ is approximately equal to $0.000001k$ and $\tilde{k}_c$ is approximately equal to $0.000001\alpha k$, where k is the spring constant and α is the nonlinear coefficient. Next, choosing a spring constant value of 100.00 N/m, and α of 100.00, the values

of $\tilde{k}_p$ and $\tilde{k}_c$ are 0.0001 and 0.001, respectively. Finally, the values of $\tilde{f}_l = -0.02$, and $\tilde{f}_c = 0.05$ are used for comparing the Ulusoy's model results to the results of the model studied in this chapter. Examining Figure 3.9, there does not seem to be much difference due to the addition of a low stifffness spring because the motions and amplitudes are close to each other in the two cases. The amplitude of the displacer with cubic spring and Ulusoy's model parameters is about 1.14 units. Likewise, the amplitude of the power piston with cubic spring and Ulusoy's model parameters is about 1.54 units. It can also be seen that the oscillation frequencies for the two models are close to each other since the motions for the two models almost overlap with each other.

However, the oscillation frequency and the amplitude can be changed by increasing or decreasing the stiffness of the system. Increasing the stiffness should decrease the amplitudes of motions of the pistons while increasing the frequency. Hence, the values for $\tilde{k}_p$ and $\tilde{k}_c$ are chosen to be 0.01. The amplitudes of the displacer and power piston, along with the oscillation frequencies are compared to the case without any spring attached to the power piston. The obtained motions for the different cases are presented in Figure 3.10. It can be seen that the amplitudes without any spring added to the power piston have higher values. The amplitudes for the displacer and power piston without any spring parameter are 1.12 units and 1.53 units, respectively. The amplitudes for the displacer and power piston with the added spring parameter are 1.07 units and 1.46 units, respectively, which are about 5.00% less. While increasing the stiffness decreased the amplitude, the oscillation frequency of the system increased. This is shown in Figure 3.11, where the frequency

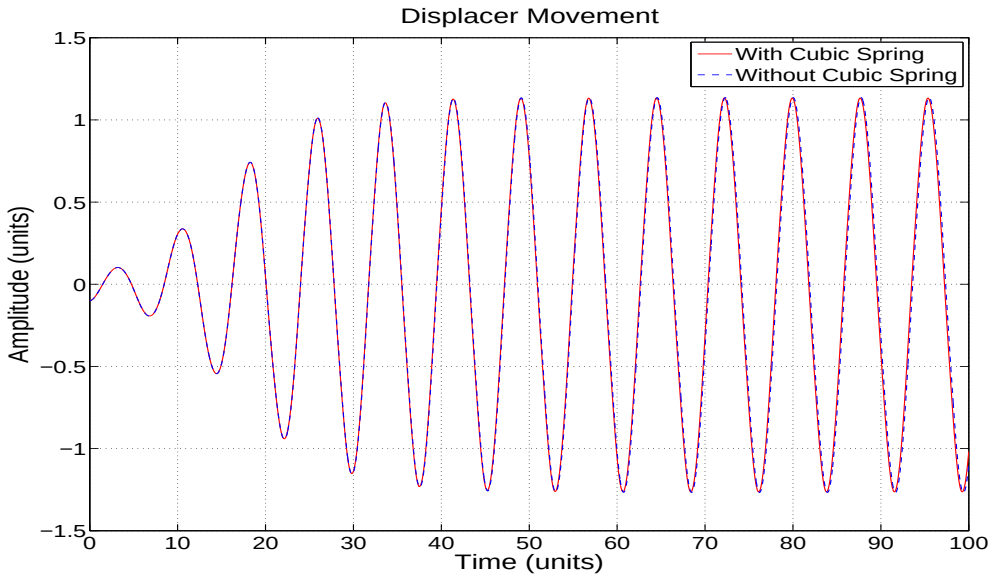

(a)

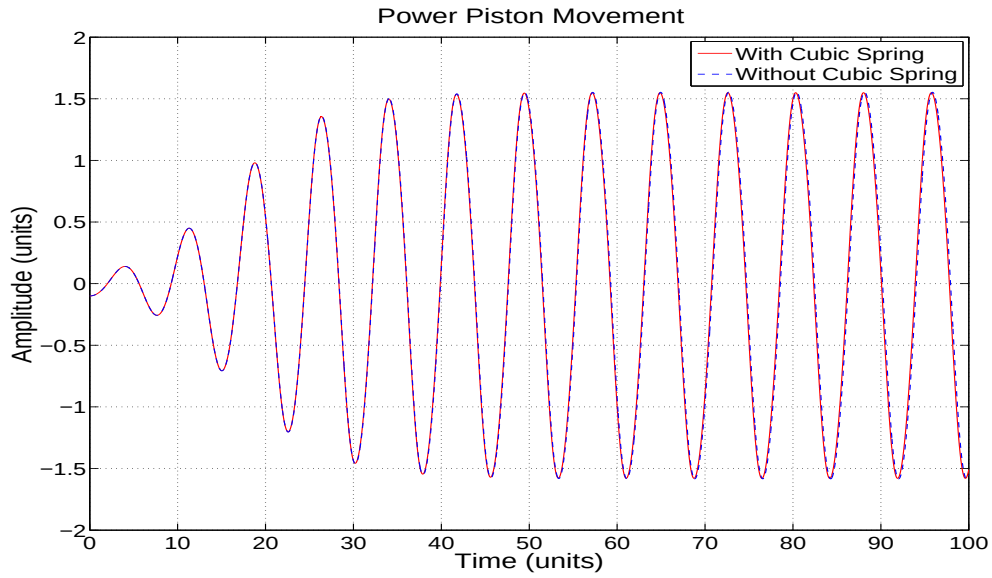

(b)

Figure 3.9: Displacement response comparison of cases with low stiffness nonlinear spring and without nonlinear spring. (a) Response of displacer and (b) Response of power piston.

spectrum for the two different cases are plotted. The oscillation frequency of the system without any spring parameter added to the power piston is about 24.20 Hz while the oscillation frequency for the added spring parameter case is 25.50 Hz; there

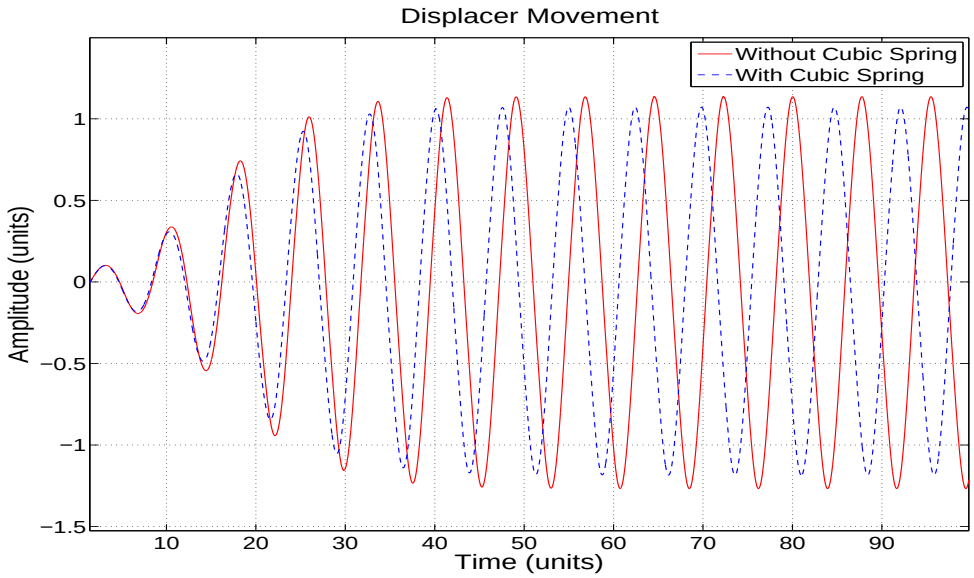

(a)

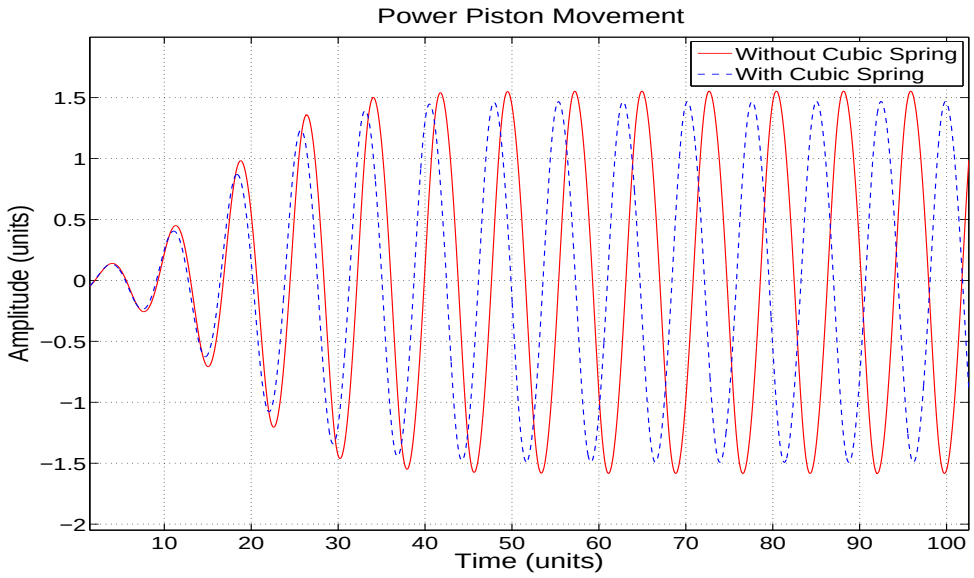

(b)

Figure 3.10: Displacement response comparison of cases with high stiffness nonlinear spring and without nonlinear spring. (a) Response of displacer and (b) Response of power piston.

is an increase of about 5.00%.

Finally in Figure 3.12, the amplitude responses of the displacer and power pistons as the linear, $\tilde{k}_p$, and nonlinear, $\tilde{k}_c$, spring parameters are varied are shown.

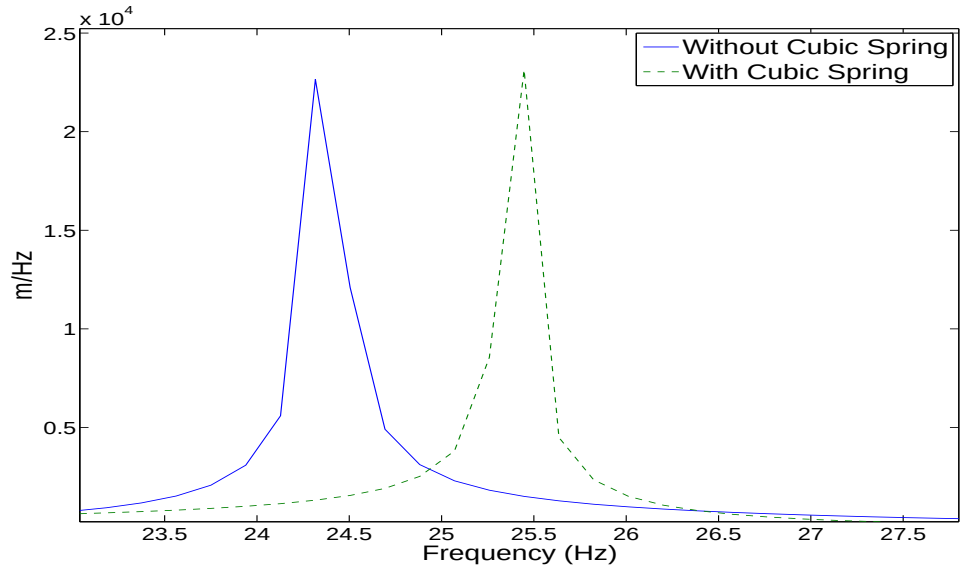

Figure 3.11: Frequency spectrum comparison for cases with and without nonlinear spring.

The linear load parameter, f_l, is held constant at -0.02. It can be seen that when the linear stiffness of the system is 0.00, the system is unstable. However, when the linear stiffness is introduced to the system, the response amplitude decreases. Increasing the linear stiffness of the system quickly decreases the response amplitude of the system to zero. However, with only a large cubic stiffness, the amplitude response variation of the system does not go to zero quickly.

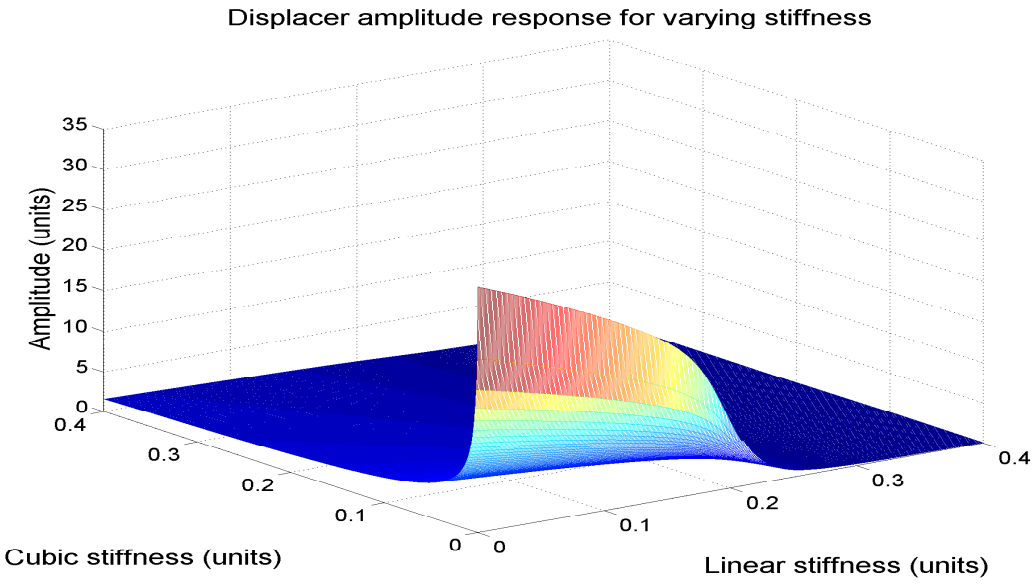

(a)

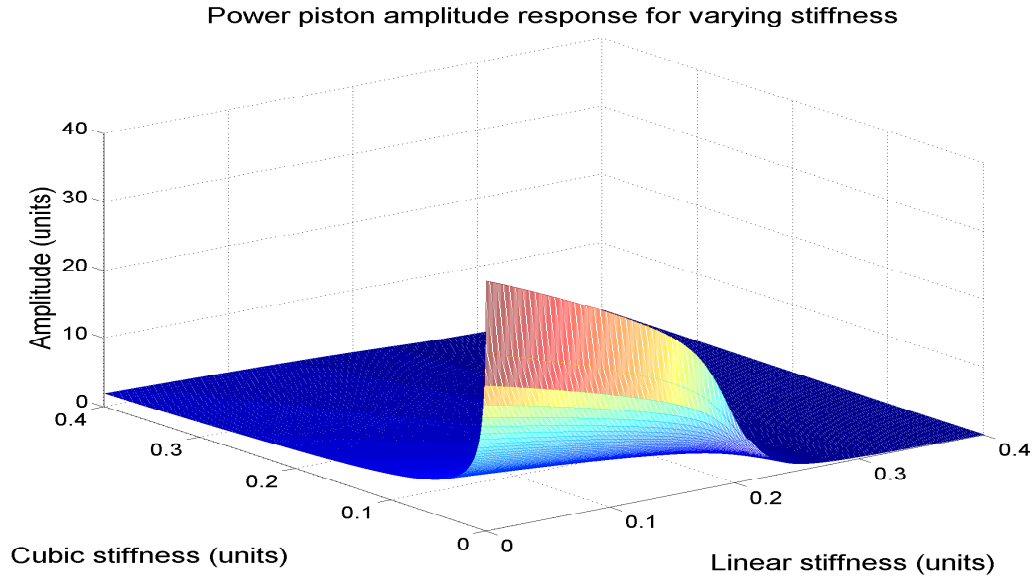

(b)

Figure 3.12: Amplitude response variation with respect to linear stiffness parameter $\tilde{k}_p$, and nonlinear stiffness parameter $\tilde{k}_c$, with linear load parameter, f_l, set to -0.02. (a) Response of displacer and (b) Response of power piston.

Chapter 4

Governing Equations for System with Magnetic Springs

Introducing nonlinearities causes the FPSE to exhibit limit-cycle motions. Previously, it was shown that nonlinear springs, especially hardening springs, also cause the system to exhibit periodic motions. Hence, magnetic springs are introduced into the FPSE, which display hardening spring behavior in one direction and softening spring behavior in another direction. The schematic for the magnetic spring FPSE is shown in Figure 4.1. Magnetic springs can be more robust than conventional springs or elastic bands because the magnetic springs would not be in contact with one another. Hence, using magnetic springs can increase the longevity of a FPSE and may make the FPSE more reliable. Also, the property of elastic bands depend

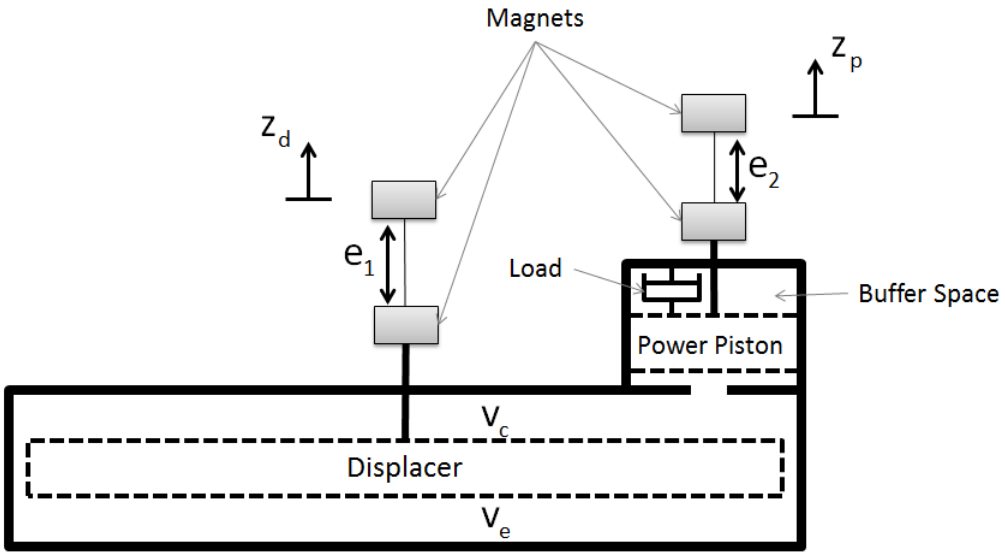

Figure 4.1: Schematic of magnetic spring FPSE.

on temperature, displacement, and time, which may give very inconsistent results. Unlike gas springs, the tolerances to use magnetic springs can be larger since they do not require the FPSE to be perfectly sealed to prevent gas leakage. Finally, the usage of magnetic springs can also reduce the operational noise in the system. Gravity must be introduced to the system in order to have restoring force for proper analysis. The magnetic spring force can be described as

$$F_{magneticspring} = Mg - F_{magnet} \tag{4.1}$$

where M is the mass of the top magnet, g is gravity, and F_{magnet} is the repulsive magnetic force. Adding gravity to the system is critical, since as the magnets are repulsed away from each other, the weight of the top magnet acts as the restoring force. A generic force curve of magnetic spring, derived in the next section, is shown in Figure 4.2. The black square in the figure represents a magnet; it can be seen that the magnetic spring behaves as a hardening spring when the upper magnet comes in close proximity with the lower magnet and as a softening spring when it goes further away from the other magnet. The equilibrium point of the magnetic spring can be varied by changing the mass of the top magnet.

The equations of motions with the magnetic spring can be written as

$$\bar{m}_d \ddot{z}_d = A_d \Delta P + F_{magnet_1} - \bar{m}_d g \tag{4.2}$$

$$\bar{m}_p \ddot{z}_p = A_p P_m \left(1 - \frac{1}{F}\right) + F_{load} \dot{z}_p + F_{magnet_2} - \bar{m}_p g \tag{4.3}$$

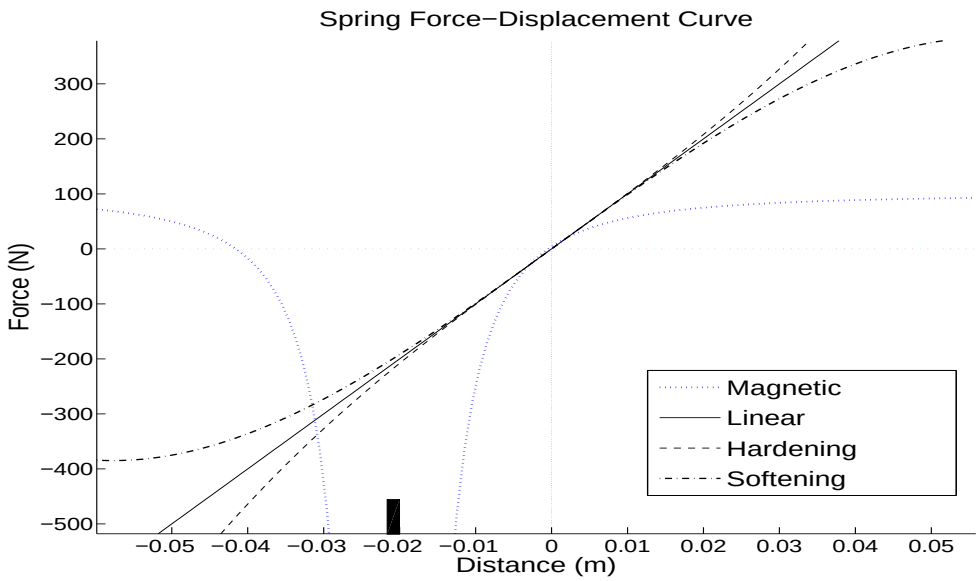

Figure 4.2: Magnetic spring force curve compared to various types of spring forces.

where

$$z_d = x_d + e1$$

$$z_p = x_d + e2$$

$$\bar{m}_d = m_d + M_1$$

$$\bar{m}_p = m_p + M_2$$

$$F_{load} = (-f_l - f_c z_p^2)$$

Furthermore, a and b are the equilibrium distances between the two repulsive magnets, M_1 and M_2 are the masses of the magnets, f_l is the linear damping parameter, and f_c is the nonlinear damping term. The equilibrium distances can be found by

setting all the velocity and acceleration terms to zero; that is

$$\bar{m}_d g = F_{magnet_1} \tag{4.4}$$

$$\bar{m}_p g = A_p P_m \left(1 - \frac{1}{F}\right) + F_{magnet_2} \tag{4.5}$$

4.1 Nondimensional Equations

In this section, the variables for the governing equations are nondimensionalized. The different quantities are as follows:

Masses:

$$\tilde{m}_d = \frac{\bar{m}_d l_d}{A_d P_m} \tag{4.6}$$

$$\tilde{m}_p = \frac{\bar{m}_p l_d}{A_d P_m} \tag{4.7}$$

Displacements:

$$\tilde{z}_d = \frac{z_d}{l_d} \tag{4.8}$$

$$\tilde{z}_p = \frac{z_p}{l_d} \tag{4.9}$$

where l_d is the length of the displacer rod.

Area:

$$\tilde{A}_d = \frac{A_d}{A_d} \tag{4.10}$$

$$\tilde{A}_p = \frac{A_p}{A_d} \tag{4.11}$$

Pressure:

$$\Delta\tilde{P} = \frac{\Delta P}{P_m} \tag{4.12}$$

$$\tilde{P}_m = \frac{P_m}{P_m} \tag{4.13}$$

Forces:

$$\tilde{F}_{magnet_1} = \frac{F_{magnet_1}}{A_d P_m} \tag{4.14}$$

$$\tilde{F}_{magnet_2} = \frac{F_{magnet_2}}{A_d P_m} \tag{4.15}$$

$$\tilde{F}_{load} = \frac{F_{load}}{A_d P_m} \tag{4.16}$$

$$\tilde{m}_d\tilde{g} = \frac{\bar{m}_d g}{A_d P_m} \tag{4.17}$$

$$\tilde{m}_p\tilde{g} = \frac{\bar{m}_p g}{A_d P_m} \tag{4.18}$$

Other quantities:

$$\tilde{a} = \frac{a}{l_d} \tag{4.19}$$

$$\tilde{b} = \frac{b}{l_d} \tag{4.20}$$

$$\tilde{F} = 1 - \tilde{a}\tilde{x}_p + \tilde{b}\tilde{x}_d \tag{4.21}$$

The nondimensional equations of motions are of the form

$$\tilde{m}_d\ddot{\tilde{z}}_d = \tilde{A}_d\Delta\tilde{P} + \tilde{F}_{magnet_1} - \tilde{m}_d\tilde{g} \tag{4.22}$$

$$\tilde{m}_p\ddot{\tilde{z}}_p = \tilde{A}_p\tilde{P}_m\left(1 - \frac{1}{\tilde{F}}\right) + \tilde{F}_{load}\dot{\tilde{z}}_p + \tilde{F}_{magnet_2} - \tilde{m}_p\tilde{g} \tag{4.23}$$

4.2 Repulsive Magnetic Forces

In order to understand how the repulsive magnetic forces behave, the principle of superposition is applied, which states that the interaction between any two charges is completely unaffected by the presence of others (Griffiths, 1999). Hence, in order to find a force on a particular charge, Q, among several charges, q_i, one must compute force F_1 due to q_1 while ignoring all other charges, then, compute force F_2 due to q_2 alone, and so forth. Finally, the total force felt by charge Q is determined as the summation of all forces. The force between any two point charges are given by Coulomb's law, which reads as

$$\mathbf{F} = \frac{1}{4\pi\epsilon_0}\frac{qQ}{r^2}\hat{r} \tag{4.24}$$

where ϵ_0 is the permittivity of free space, q is the source charges, Q is the test charge, r is the distance between the two charges, and $\hat{r}$ is the associated unit vector. The force is repulsive if q and Q have the same sign, and attractive if they have opposite signs. Finally, for several point charges q_1, q_2,...,q_n at distances r_1, r_2,...,r_n from Q, the total force on Q is given by (Griffiths, 1999)

$$\mathbf{F} = \mathbf{F}_1 + \mathbf{F}_2 + ... = \frac{1}{4\pi\epsilon_0}\left(\frac{q_1 Q}{r_1^2}\hat{r}_1 + \frac{q_2 Q}{r_2^2}\hat{r}_2 + ...\right) \tag{4.25}$$

$$\mathbf{F} = \frac{Q}{4\pi\epsilon_0}\left(\frac{q_1}{r_1^2}\hat{r}_1 + \frac{q_2}{r_2^2}\hat{r}_2 + ...\right) \tag{4.26}$$

$$\mathbf{F} = QE \tag{4.27}$$

where E is the electric field of the charges and is defined as:

$$\mathbf{E} = C\left(\sum_{i=1}^{n} \frac{q_i}{r_i^2}\hat{r}_i\right) \tag{4.28}$$

and

$$C = \frac{1}{4\pi\epsilon_0} \tag{4.29}$$

Next, each magnet used here is modeled as magnetic dipole, or a set of two charges as shown in Figure 4.3. As such, the charge is defined as

$$\int_S \epsilon_0 M dA = -q_i \tag{4.30}$$

where S is a closed surface area, q_i is the charge enclose within that area, and M is the magnetization. The charge is defined as negative because the magnetic field moves from positive to negative charge (Griffiths, 1999). Integrating over a circular surface area leads to

$$q_i = -\epsilon_0 M \pi R^2 \tag{4.31}$$

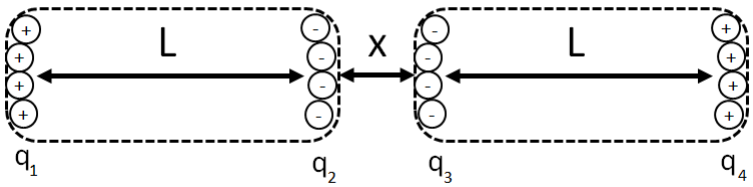

Figure 4.3: Magnets modeled as charges.

which is negative for a negative charge source, but positive for a positive charge source.

Assuming constant radius, the forces between each charge from one magnet to another are found and then summed as follows

$$F_{q_1,q_3} = C\frac{q_1 q_3}{(x+L)^2} \tag{4.32}$$

$$F_{q_1,q_4} = C\frac{q_1 q_4}{(x+2L)^2} \tag{4.33}$$

$$F_{q_2,q_3} = C\frac{q_2 q_3}{(x)^2} \tag{4.34}$$

$$F_{q_2,q_4} = C\frac{q_2 q_4}{(x+L)^2} \tag{4.35}$$

After using equation (4.31), an approximation for the repulsive magnetic force can be found as

$$\sum F = \frac{\pi\epsilon_0}{4} M^2 R^4 \left[\frac{1}{x^2} + \frac{1}{(x+2L)^2} - \frac{2}{(x+L)^2}\right] \tag{4.36}$$

The force-displacement curve of the repulsive magnetic spring is shown in Figure 4.4. The dotted points are the representative force given by the manufacturer KJ-Magnetics, while the other line is the model prediction curve. Both curves follow a similar profile; also, the range of motion for the numerical and experimental studies is greater than 1.00 cm. Large values for the constant will make the magnetic spring stiffer, while small values will make the magnetic spring softer.

Equation (4.36) is compared to the magnetic force derived by Vokoun, Beleggia, Heller, and Sittner (2009). They derive the force between sets of magnets from

the total magnetostatic interaction energy E of the system, which is given by:

$$F_{mag} = -grad(E) \tag{4.37}$$

The assumptions made are that the magnets are cylindrical and that they are made of the same material characterized by saturation magnetization M. The cylindrical magnets are of equal radius R and are magnetized uniformly along the cylinder axis of symmetry. The force between two cylindrical permanent magnets with a common axis is derived to be (Vokoun *et al.*, 2009)

$$F_{magnet} = \frac{\pi\mu_0}{4} M^2 R^4 \left[\frac{1}{x^2} + \frac{1}{(x+2t)^2} - \frac{2}{(x+t)^2} \right] \tag{4.38}$$

where M is the magnetization, R is the radius of the magnet, t is the height of the magnet, and μ_0 is the permeability of vacuum. Comparing equations (4.36) and

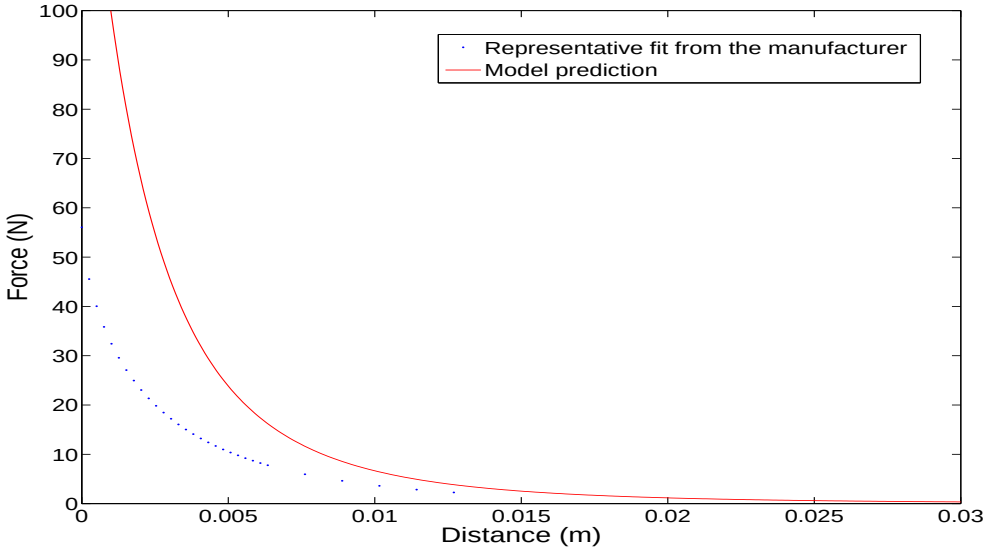

Figure 4.4: Repulsive force between two similar magnets.

(4.38), it can be seen that the equations are similar.

By using Equations (2.43), (4.22), and (4.23), the nondimensionalized equations of motion for the system with the magnetic spring can be written as

$$\tilde{m}_d \ddot{\tilde{x}}_d = \frac{\tilde{A}_d}{P_m}\left[\frac{1}{2}\rho\left(f_t + k_h\right)\frac{2A_d\dot{z}_d - A_p\dot{z}_p}{A_k}\left|\frac{2A_d\dot{z}_d - A_p\dot{z}_p}{A_k}\right| + \frac{\pi\mu_0 M_d^2 R_d^4}{4A_d P_m}\left[\frac{1}{z_d^2} + \frac{1}{(z_d+2t)^2} - \frac{2}{(z_d+t)^2}\right] - \tilde{m}_d\tilde{g}\right. \quad (4.39)$$

$$\tilde{m}_p \ddot{\tilde{x}}_p = \tilde{A}_p\left(1 - \frac{1}{F}\right) + \tilde{F}_{load}\dot{\tilde{z}}_p + \frac{\pi\mu_0 M_p^2 R_p^4}{4A_d P_m}\left[\frac{1}{z_p^2} + \frac{1}{(z_p+2t)^2} - \frac{2}{(z_p+t)^2}\right] - \tilde{m}_p\tilde{g} \quad (4.40)$$

Here A_k is the area of the annulus between the displacer and the wall in Figure 4.1 through which the working fluid is displaced.

4.3 Results for System Response

In this section, various findings for the modified system with modeled pressure loss is presented. The parameters used for the modeling are presented in Appendix B. First, the magnetic spring case without any damping is shown. Then, the head loss within the annulus and damping is introduced.

The movements of the displacer and power piston without any damping can be seen in Figure 4.5. The initial condition given to the system is (0.01 0.0 0.0 0.0). Although damping is not present, the system shows oscillatory motions. This is further verified through the phase portrait diagram shown in Figure 4.6. The power

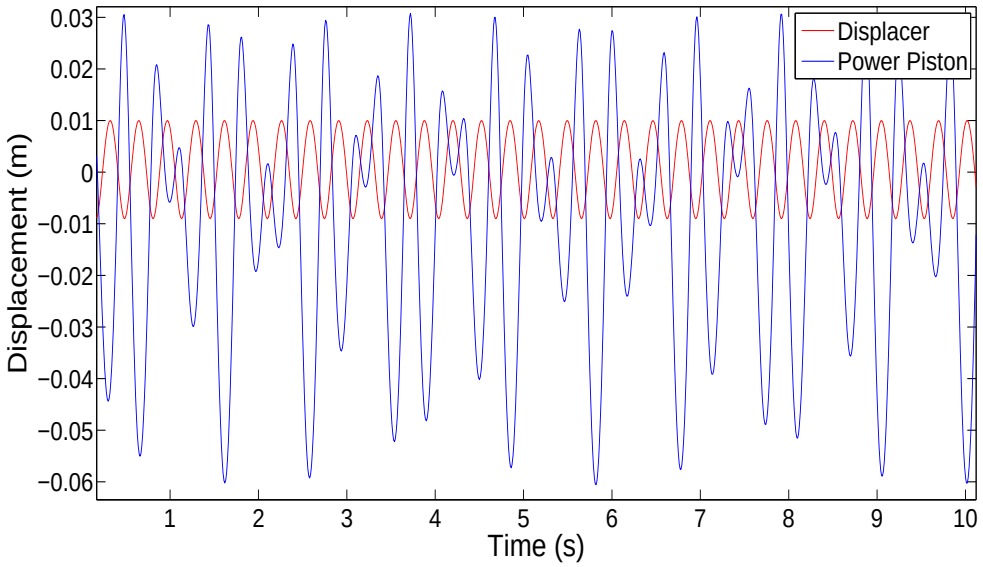

Figure 4.5: Displacement response of magnetic spring FPSE without any damping or head loss.

piston does not follow the movements of the displacer, which shows that there is a weak coupling between the two pistons.

Next, a low level of damping and head loss is introduced into the power piston. The linear damping term f_l is chosen to be 0.01, the cubic nonlinear term f_c is set at 0.02, and the head loss k_h is set at 0.05. The initial condition is held constant at

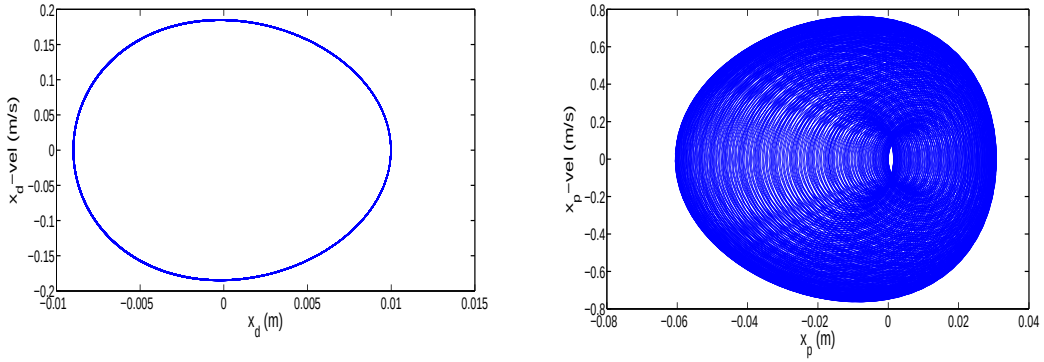

(a) (b)

Figure 4.6: Phase portraits for the case with no damping and with ICs: (0.01 0.0 0.0 0.0). (a) Displacer and (b) Power Piston.

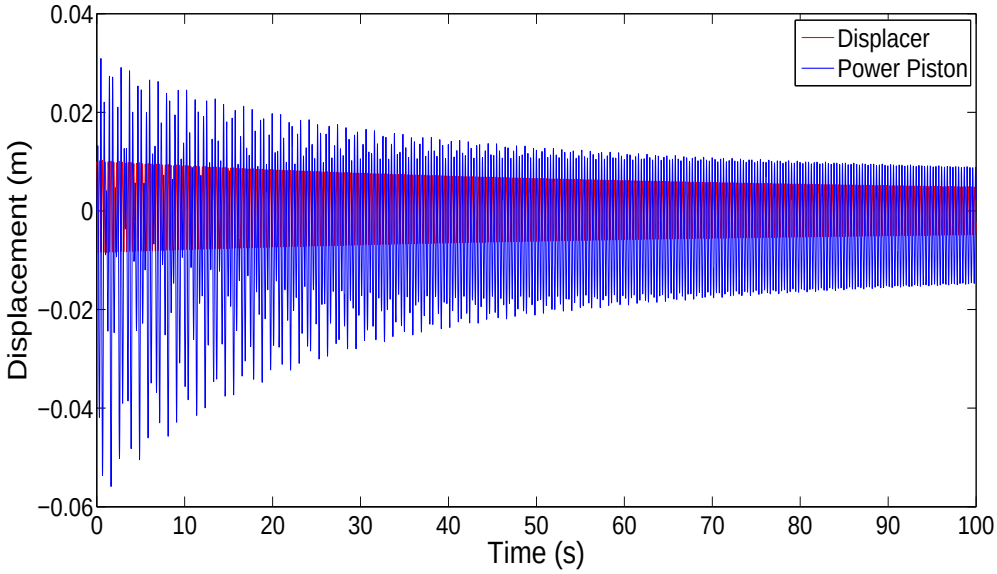

Figure 4.7: Displacement response of magnetic spring FPSE with low damping and head loss.

their previous values. The amplitudes for the displacer and power piston are shown in Figure 4.7. As expected, the amplitudes decrease with damping. Once again, the phase portrait is shown to verify oscillatory motions in Figure 4.8.

Finally, the damping parameter is increased to verify that the amplitudes die out when the system is highly damped. The linear damping term f_l is chosen to

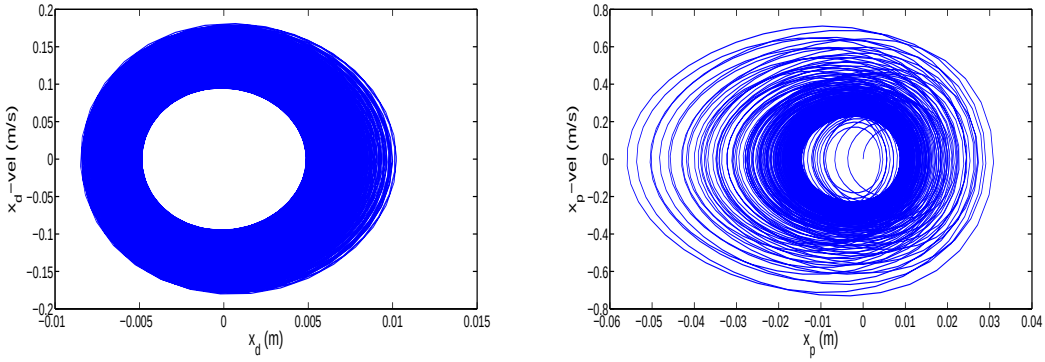

(a) (b)

Figure 4.8: Phase portraits for the case with low damping and head loss and with ICs: (0.01 0.0 0.0 0.0). (a) Displacer and (b) Power Piston.

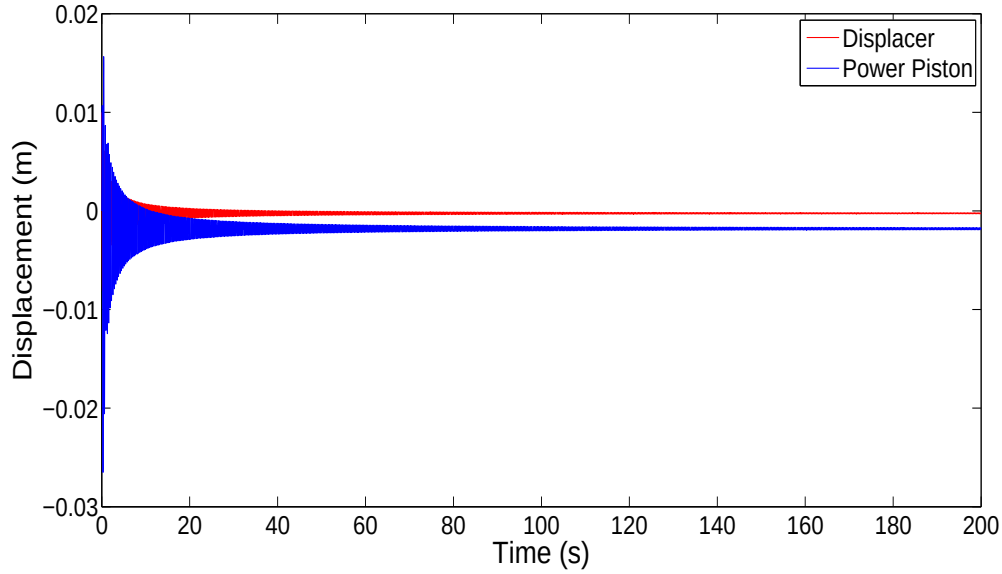

Figure 4.9: Displacement response of magnetic spring FPSE with high damping and head loss.

be 0.50, the cubic nonlinear term f_c is set at 0.50, and the head loss k_h is set at 5.00. From Figure 4.9, it can be seen that the amplitudes for both the displacer and the power piston die out with large damping. However, when the temperature

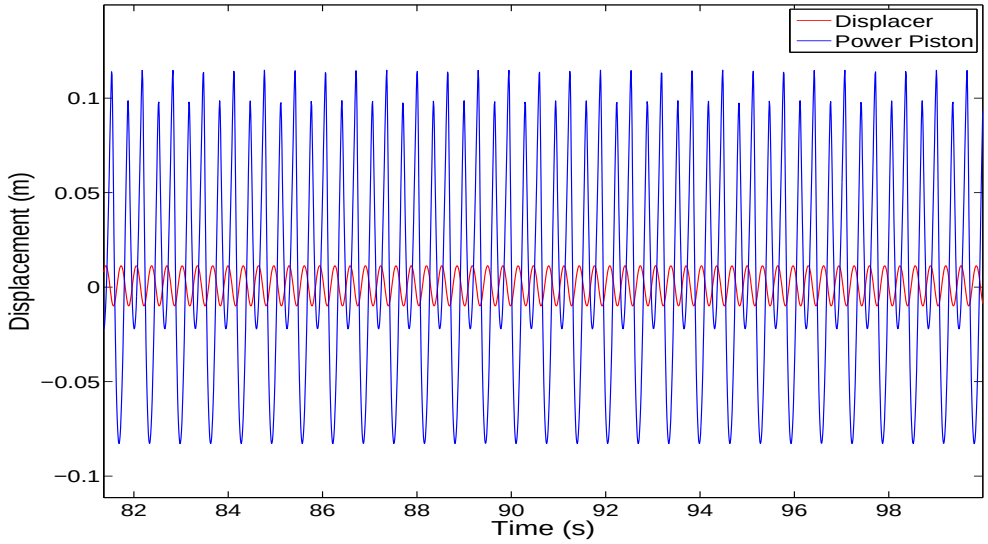

Figure 4.10: Displacement response of magnetic spring FPSE with high damping and head loss with temperature difference of 500.00° Celcius.

difference between the expansion space and compression space is increased to 500.00° Celsius, the system response shows oscillatory motion as shown in Figure 4.10. The numerical studies of this chapter indicate that with a magnetic spring, a FPSE may not show oscillatory motions due to high levels of damping. However, this may be overcome with an appropriate temperature gradient. In addition, further work is needed to realize limit-cycle motions in a FPSE with magnetic springs.

Chapter 5

Experimental Studies

In this chapter, experimental studies conducted in an attempt to realize a FPSE system are presented. Various configurations of the FPSE are designed for the possibilities of having oscillatory motions. The kinematic Stirling engine shown in Figure 5.1 is modified and turned into a FPSE. The flywheel connecting the power piston and the displacer are disconnected and replaced with magnets to levitate the power piston and the displacer. The power piston is fabricated from graphite, and the compression volume around the power piston is made of borosilicate glass in order to reduce friction.

The schematic of the experimental setup is shown in Figure 5.2. The power source is connected to the temperature controller, which controls the thermoelectric

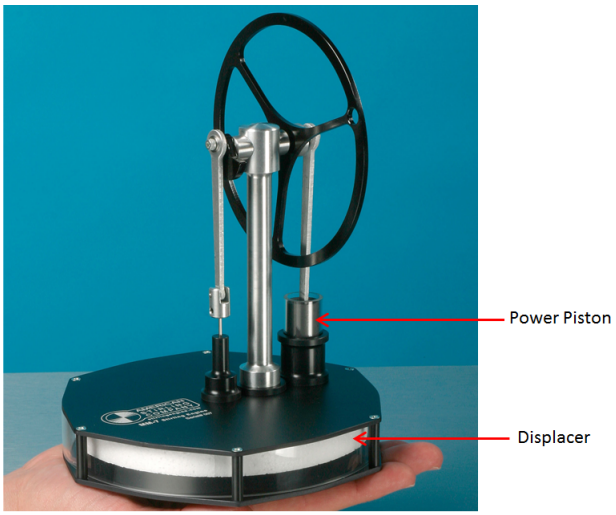

Figure 5.1: Kinematic Stirling engine to be modified into FPSE.

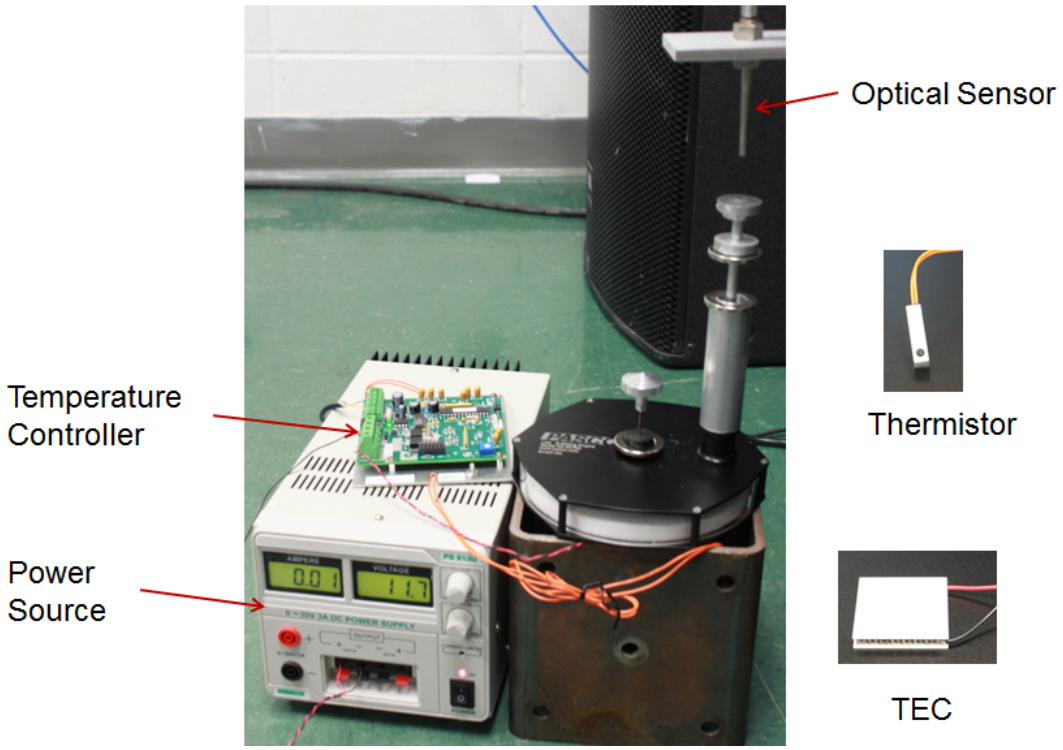

Figure 5.2: Schematic of the experimental setup.

cooler (TEC) and the thermistor. Both, the TEC and the thermistor are attached to the bottom of the FPSE. The TEC can be controlled to vary the temperature of the expansion space of FPSE while the thermistor is used to measure the temperature. At the top, a fiber optic sensor is used to measure the movement of the power piston.

5.1 Design and Fabrication

The first iteration of the experimental setup is shown in Figure 5.3. The rod connecting the power piston to the magnet, along with the magnet holders were fabricated by this thesis author. The top magnets are attached to the magnet holders via a press fit. The holders are designed to be adjustable so that it can slide up and down. This way, the equilibrium point can be adjusted by adding weights

such that the displacer and power piston sit at the middle of the expansion and compression space, respectively. In this setup, the magnetic interference between the two magnetic springs are found to be high because of their close proximity; thus, introducing high damping into the system due to eddy currents. The repulsion and attraction between the top magnet for the displacer and the magnets for the power piston cause the displacer rod to bend slightly either towards or away from the the power piston. This increases the friction between the displacer rod and its casing. Similarly, interactions between the displacer and the power piston magnets increase the friction between the power piston and its casing.

In order to reduce the magnetic interference and decrease piston rod related damping, the magnetic spring for the power piston is elevated. The modified schematic is shown in Figure 5.4. A tube that encased the power piston was fabricated, and the rod connecting the power piston was made longer. However, the dimensions and the placement of the power piston were kept the same as that of the

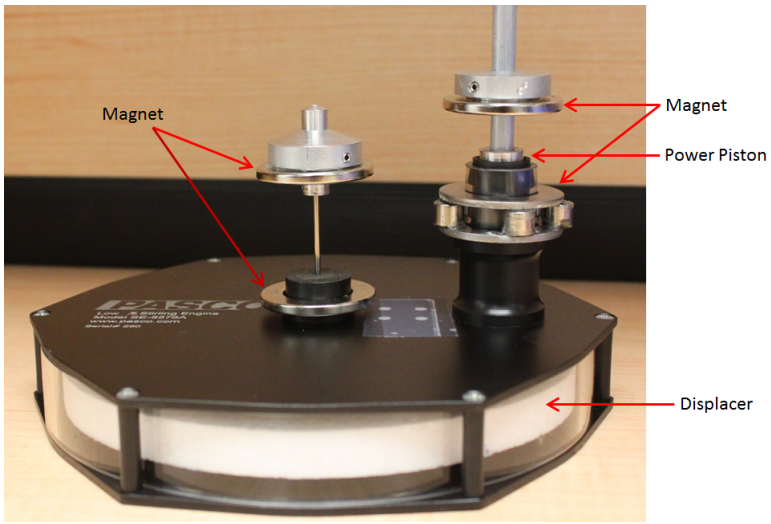

Figure 5.3: Modified FPSE.

previous configuration. Increasing the height of the power piston rod had adverse affects. The weight of the magnet and the holder for the power piston caused the power piston rod to tilt. This increased the normal force between the power piston and the casing, which in turn increased the friction. Another problem that was also noticed was that the displacer had very little room for movement. Hence, when the displacer moved, it tended to stick to the top or the bottom of the casing. When the displacer sticks to the top, it closes the path for the air to get into compression space; hence, the air is prevented from being compressed. Likewise, when the displacer sticks to the bottom, the air is prevented from being expanded.

Finally, the expansion space was doubled so that the displacer could have more room for oscillations. This configuration is shown in Figure 5.5. Again, this configuration did not produce oscillatory motions. One of the reasons might be that the compression space is small compared to that of the expansion space. Thus, when

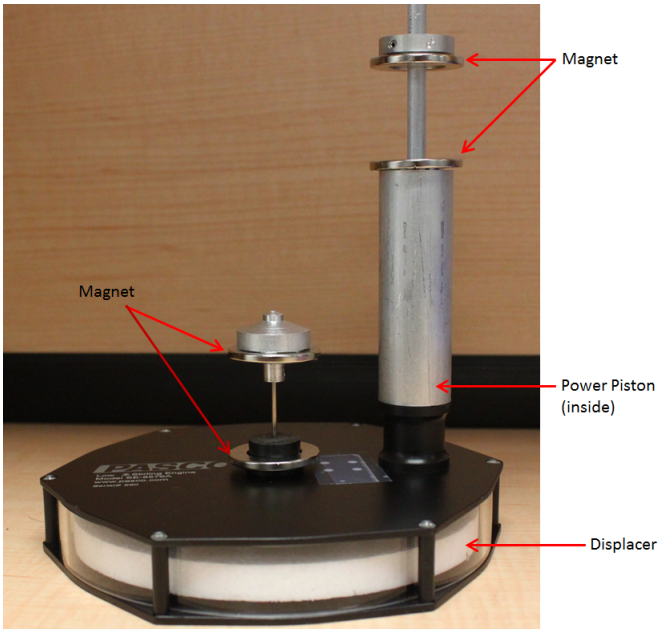

Figure 5.4: Increased height for the power piston.

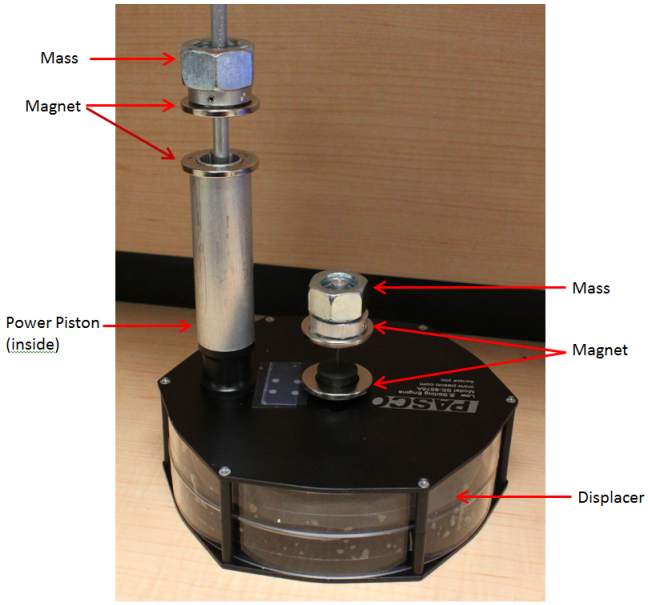

Figure 5.5: Increased volume for the expansion space.

the compression space collapses, the decrease in volume does not lead to a sufficient pressure increase in the compression area. Hence, the pressure difference across the displacer does not increase very much.

5.2 Preliminary Experimental Results

The different configurations were heated to about 315.00° Celsius while the cold end of the engine was at room temperature of about 25.00° Celsius. The parameters for the experimental setup are given in Appendix B. The response obtained for the kinematically linked Stirling engine is shown in Figure 5.6. For this system, oscillatory motions are observed. The frequency of the system is about 6.20 Hz.

For the first modified system depicted in Figure 5.3, the displacer and power piston motions decay right away. The motion of the power piston was captured using a Philtec optical sensor, and the observed response is shown in Figure 5.7.

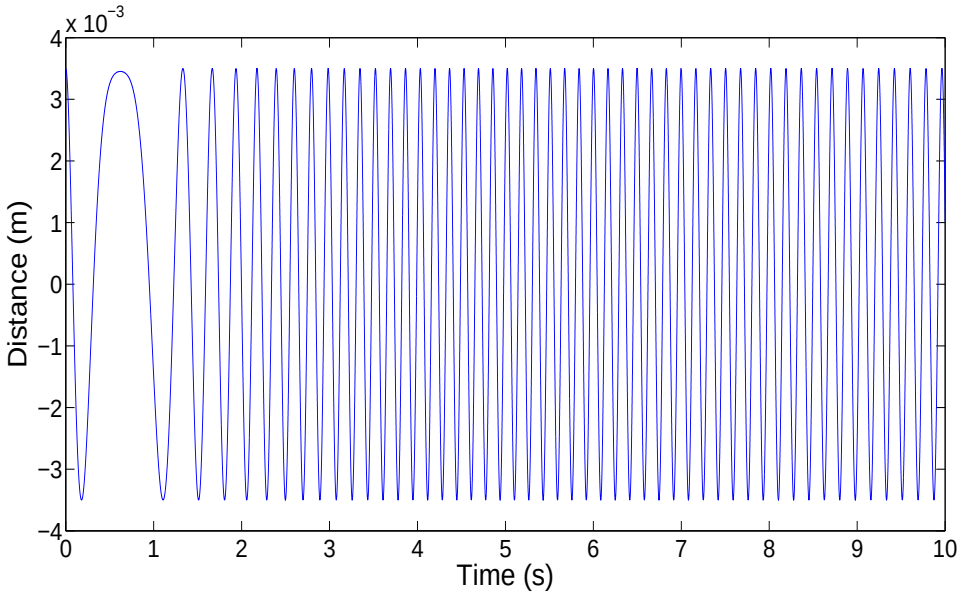

Figure 5.6: Power piston displacements for a kinematically linked Stirling engine.

Due to high damping, the decaying motion is as expected. By using the data along with the logarithmic decrement method, the damping ratio is approximated to be 0.31, and the undamped frequency is 1.59 Hz.

For the second modified system depicted in Figure 5.8, the power piston os-

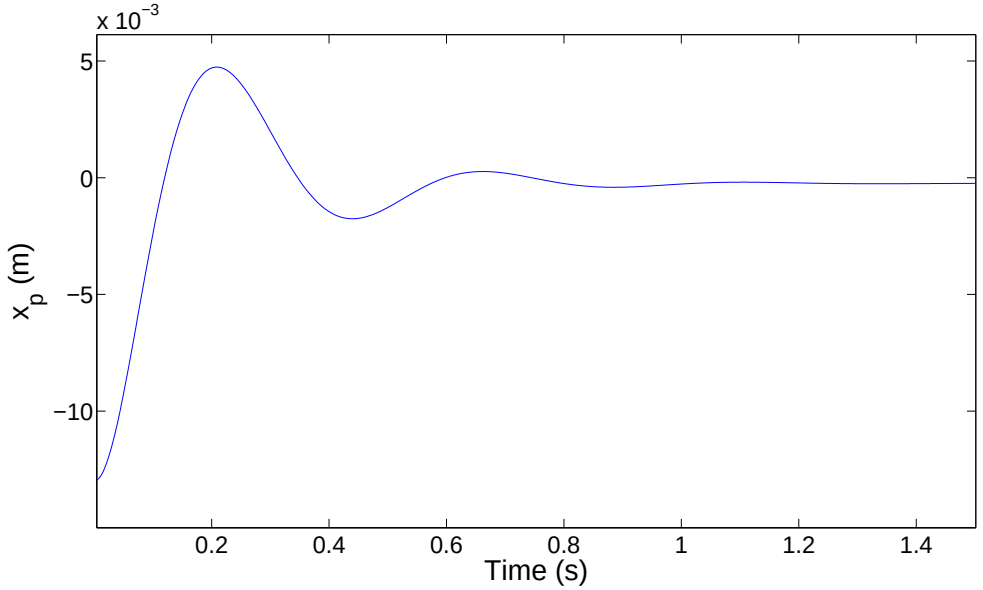

Figure 5.7: Power piston displacements for first FPSE arrangement.

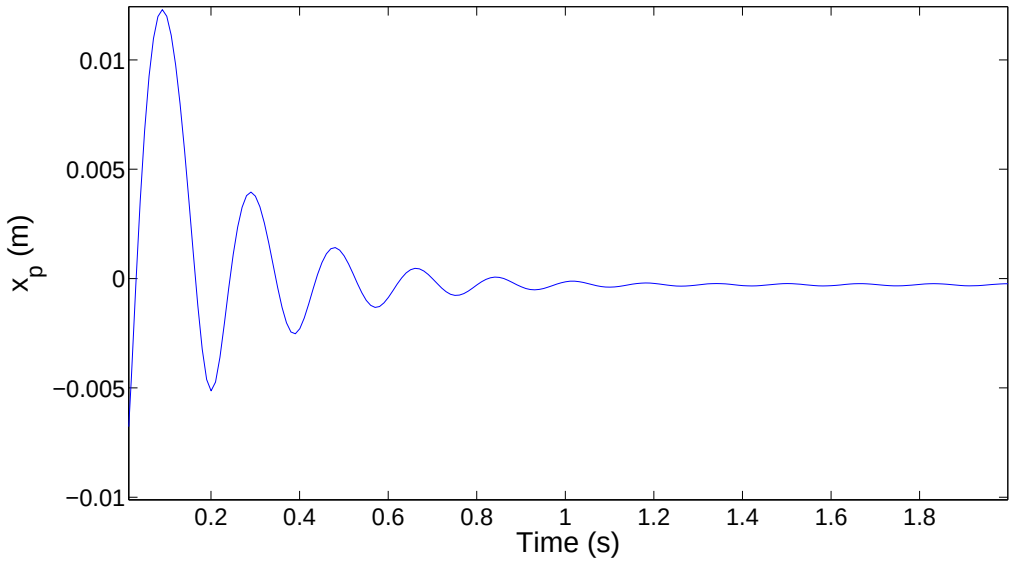

Figure 5.8: Power piston displacements for second FPSE arrangement.

cillates very little and decays again. The oscillation of the power piston is shown in Figure 5.8. Again, the decaying oscillations are due to the high damping inherent in the system due to the design. The damping ratio approximated for the configuration is 0.21, and the undamped frequncy is 5.60 Hz. The last configuration did not provide any positive results either as the decaying motions were very similar to the previous configuration. The numerical studies of the previous chapter support the observations made in this chapter; that is, a high damping level can inhibit oscillatory motions. Future experiments can be conducted with a higher temperature gradient to see if that would help in realizing oscillatory motions.

Chapter 6

Summary and Concluding Remarks

A FPSE has various advantages over kinematically linked Stirling engines; as such, FPSEs would be better for practical purposes. A kinematically linked Stirling engine relies on the linkage between the displacer and power piston for its motions. A FPSE rely solely on the pressure difference created by the temperature gradient and volume variations. Various parameters within the FPSE are critical for its functionality. Hence, parametric studies have been conducted to study which parameters can help the system exhibit oscillatory motions. Additionally, a study of a nonlinear system with a spring attached to the power piston is conducted. The considered beta engine exhibits Hopf instabilities with a hardening spring on the power piston side and the introduction of nonlinear spring leads to limit-cycle motions. Next, magnetic springs are introduced into the FPSE system, and the motions of the displacer and the power piston are studied. The system with magnetic springs shows oscillatory motions. Finally, experimental studies are conducted in an attempt to show oscillatory responses for a FPSE. The significance of this thesis work is the understanding developed on Hopf instabilities in FPSEs. Also, the experimental studies help understand difficulties in realizing a FPSE from a kinematic Stirling engine. This thesis study complements the analytical-numerical work conducted in the group by Choudhary (2009).

6.1 Parametric Studies

The model studied by Ulusoy (1994) is modified to include spring term ($\tilde{k}_p$) for the power piston. With the introduction of the spring parameter, the Jacobian matrix of the system is investigated. By using the characteristic equation found from the Jacobian, a parametric study is conducted by varying the spring parameter, $\tilde{k}_p$, and the damping parameter, $\tilde{f}_l$. It is shown that a Hopf instability can be attained by varying the damping parameter, while the spring parameter is zero. Additionally, one can have a Hopf instability in the absence of the system damping due to the spring parameter as well. The influences of the damping parameter and the spring parameter are established. With increasing stiffness in the system, it is found that the system damping needs to be reduced for oscillatory motions to occur.

Next, a nonlinear hardening spring is introduced into the power piston. The system response is unstable for a case with linear damping. However, the addition of the nonlinear spring leads to oscillatory motions. Introducing the spring to the system affected the amplitude and the oscillatory frequency of the system. Comparing the motions of FPSE without nonlinear spring added to the power piston to the system with a low stiffness nonlinear spring added to the power piston showed that the amplitude between the two does differ by much. By increasing the stiffness of the spring, the response amplitude decreases but the oscillation frequency increases. The advantage realized by adding a nonlinear spring to the power piston is to realize limit-cycle motion in a FPSE without a cubic damper, while also being able to vary the oscillatory frequency of the system.

6.2 System with Magnetic Springs

Once it was found that nonlinear spring helps attain oscillatory motions, magnetic springs were introduced into the system. The advantages of the inclusion of magnetic springs in a FPSE are less friction leading to higher durability and less operational noise. The repulsive forces between two magnets are found by modeling the charges as dipole moments along with Coulomb's law. The numerical results obtained for the magnetic spring model showed that the displacer and the power piston are weakly linked. The results showed that oscillatory motions are possible with magnetic springs. However, with very high damping, the motions die out. In order to overcome large damping, a high temperature difference between the expansion and the compression space is necessary.

6.3 Experimental Studies

Various configurations for FPSE were designed and fabricated in an attempt to realize oscillatory motions. The first modified configuration shown in Figure 5.7 had very high damping due to the proximity of the magnets used in the displacer and power pistons. Hence, the motions decay quickly. This configuration was modified as shown in Figure 5.8. The new design created high friction between the power piston and the casing along with the displacer sticking to the hot end and cold end of the FPSE. Therefore, this configuration did not exhibit oscillatory motions either. Finally, the expansion volume was expanded to overcome the sticking problem. This modification did not result in oscillatory motions either. It is suspected that

the damping levels in the experimental system may not be appropriate to realize oscillatory motions; a large temperature difference between the expansion and the compression space would be needed to realize oscillatory motions. The experimental studies also helped realize the difficulties in fabricating a FPSE from a kinematically linked Stirling engine.

6.4 Future Work

The present thesis work supports the promise of realizing low power FPSEs. However, further analytical and numerical studies are needed to understand the nature of Hopf instabilities. NASA has previously considered Stirling engines for space applications. For these applications, the current system with magnetic springs, which relies on gravity will not work. In order to overcome this, the design of the magnetic springs can be changed to have a magnet repel in between two different magnets, which also makes the magnetic spring stiff from both directions. Additionally, the experiments were not successful in realizing oscillatory motions. The experimental setup should be redesigned to reduce the affect of damping in order to realize oscillatory motions. Also, various other designs for FPSEs need to be considered and appropriate parametric studies need to be conducted.

Appendix A

Equations of Motion and Parameters from Ulusoy (1994)

Equations of Motion:

The schematic of the FPSE that Ulusoy (1994) studied is shown in Figure A.1. The equations of motions for this system are given by

$$m_d \ddot{x}_d = A_d(P_c - P_e) - A_r(P_c - P_s) \tag{A.1}$$

$$m_p \ddot{x}_p = A_p(P_b - P_c) + F_{load}\dot{x}_p \tag{A.2}$$

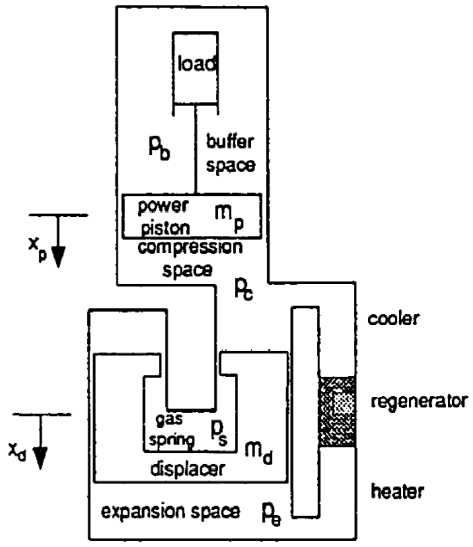

Figure A.1: Schematic of FPSE from Ulusoy (1994).

The equations of motions resulting after Schimdt analysis are as follows

$$\ddot{x}_d = \frac{A_d}{m_d}\Delta P - \frac{A_r P_m}{m_d}\left(F - \left(\frac{1}{1+a_s x_d}\right)^{\gamma}\right) \tag{A.3}$$

$$\ddot{x}_p = \frac{A_p P_m}{m_p}(1-F) + \frac{F_{load}}{m_p} \tag{A.4}$$

where

$$F = \frac{1}{1 - a_p x_p + a_d x_d} \tag{A.5}$$

$$F_{load} = \left(f_L - f_c x_p^2)\dot{x}_p\right) \tag{A.6}$$

Next the parameters are nondimensionalized. These parameters are given by

$$\tilde{x}_p = \frac{x_d}{l_p/2} \tag{A.7}$$

$$\tilde{x}_p = \frac{x_p}{l_p/2} \tag{A.8}$$

$$\tilde{P} = \frac{P}{P_m} = \frac{1}{1 - \tilde{a}_p\tilde{x}_p + \tilde{a}_d\tilde{x}_d} \tag{A.9}$$

$$\tilde{a}_p = a_p\frac{l_p}{2} \tag{A.10}$$

$$\tilde{a}_d = a_d\frac{l_p}{2} \tag{A.11}$$

$$\tilde{P}_c = P_c/P_m = \tilde{P} \tag{A.12}$$

$$\triangle\tilde{P} = \frac{\triangle P}{P_m} \tag{A.13}$$

$$\tilde{P}_e = P_c/P_m = \tilde{P} - \triangle\tilde{P} \tag{A.14}$$

$$\tilde{P}_s = P_s/P_m = \left(\frac{1}{1+\tilde{a}_s\tilde{x}_d}\right)^{\gamma} \tag{A.15}$$

$$\tilde{a}_s = a_s \frac{lp}{2} \tag{A.16}$$

$$\tilde{m}_d = \frac{\omega^2 \frac{lp}{2} m_d}{P_m A_p} \tag{A.17}$$

$$\tilde{m}_p = \frac{\omega^2 \frac{lp}{2} m_p}{P_m A_p} \tag{A.18}$$

$$\tilde{A}_d = A_d / A_p \tag{A.19}$$

$$\tilde{A}_r = A_r / A_p \tag{A.20}$$

$$\tilde{A}_p = A_p / A_p = 1 \tag{A.21}$$

$$\tilde{F}_{load} = \left(\tilde{f}_L - \tilde{f}_c x_3^2 \right) x_4 \tag{A.22}$$

$$\tilde{f}_L = \frac{f_L \omega \frac{lp}{2}}{P_m A_p} \tag{A.23}$$

$$\tilde{f}_c = \frac{f_c \omega \left(\frac{lp}{2}\right)^3}{P_m A_p} \tag{A.24}$$

$$\tilde{k}_p = \frac{k_p \frac{lp}{2}}{P_m A_p} \tag{A.25}$$

where l_p is the maximum stroke of the power piston. Hence, the nondimensional equations become:

$$\ddot{\tilde{x}}_d = \frac{\tilde{A}_d}{\tilde{m}_d} \Delta \tilde{P} - \frac{\tilde{A}_r}{\tilde{m}_d} \left(\tilde{F} - \left(\frac{1}{1 + \tilde{a}_s \tilde{x}_d} \right)^\gamma \right) \tag{A.26}$$

$$\ddot{\tilde{x}}_p = \frac{1}{\tilde{m}_p} \left(1 - \tilde{F} \right) + \frac{\tilde{F}_{load}}{\tilde{m}_p} \tag{A.27}$$

Ulusoy's Parameters:

The parameters used in his work are provided next.

Temperatures (K):

Th = 900

Tk = 300

Masses (kg):

Power Piston Mass (mp) = 6.2

Displacer Mass (md) = 0.426

Volumes (m^3):

Displacer Gas Spring Mean Volume (V_so) = $31.8 * (10^-6)$

Compression Space Mean Volume (Vco)= $103.6 * (10^-6)$

Expansion Space Mean Volume (Veo) = $63.6 * (10^-6)$

Heater Volume (Vh)= $27.309 * (10^-6)$

Cooler Volume (Vk)= $20.422 * (10^-6)$

Regenerator Volume (Vr)= $186.534 * (10^-6)$

Design Frequency (Hz)= 30

Piston length stroke (cm) =4.20

Mean Pressure (Pa) = 7,000,000

Appendix B

Experimental Parameters

The parameters corresponding to the FPSEs studied in the Vibrations Laboratory are provided below.

Masses (kg)

md = 0.001

mp = 0.001

mda = 0.1

mpa = 0.1

mdt = md+mda

mpt = mp+mpa

Length (m)

ld= 21/1000

Area (m^2)

Ad= $pi * (140/2000)^2$

Ap= $pi * (35/2000)^2$

Ak= $pi * (150/2000)^2$

Ah = $pi * (150/2000)^2$

Temperatures (K)

Th = 315 + 273

Tk = 25 + 273

Volumes (m^3)

Vcm = $pi * (35/2000)^2 * (20/1000) + pi * (152/2000)^2 * (10/1000)$

Vem = $pi * (152/2000)^2 * (13/1000)$

Pressures (Pa)

Pm = 101500

Magnets

mu =$4 * pi * (10^-7)$

Bo = 1.3200 (T)

R = 0.0254 (m)

t = 0.003175 (m)

M = $(2 * Bo/mu)$

Other Parameters

g=9.81 (m/s^2)

rho=1

Do= .152 (m)

Di= .139 (m)

L=10/1000 (m)

Appendix C

Matlab Codes

Representative programs used in this thesis study are included in this Appendix.

```
% Parametric study

close all
clear all
clc

format short

b=zeros(100,5);
t=1;
n=0;
for kp=0
    n=n+1;
    figure(n);
    tic
    for i=-1:.01:0
        A=[0 1 0 0; -.389 -1.598 -1.302 1.182; 0 0 0 1; 0.614 0 -1.056-
(kp/0.257) i/0.257];
%       A=[0 1 0 0; -.389 -1.598 -1.302 1.182; 0 0 0 1; 0.614 0 -1.0171-
(kp/0.257) i/0.257];
        c=eig(A);
%         figure(n)
        scatter(real(c),imag(c),'.')
        hold on
        b(t,1)=i;
        b(t,2)=c(1,1);
        b(t,3)=c(2,1);
        b(t,4)=c(3,1);
        b(t,5)=c(4,1);
        t=1+t;
    end
    ti=title(['Root Locus, kp=' num2str(kp)]);
    x=xlabel('Real'); y=ylabel('Imaginary');
    set(ti,'Fontsize',12)
    set(x,'Fontsize',12)
    set(y,'Fontsize',12)
    axis on
    grid on
    toc
end
```

```
%%Solving for magnetic equilibriums

u=4*Pi*10^-7;
R=.0254;
t=0.003174;
B=1.32;
M=(2*B/u);
Ap=Pi*(45/1000)^2;
Ad=Pi*(140/1000)^2;
Vcm=Pi*(45/1000)^2*(8/1000);
Vem=Pi*(145/1000)^2*(10/1000);
Pm= 500;
Tk=273+0;
Th=500+100;
S=Vem/Th+Vcm/Tk;
a=Ap/Tk(1/S);
b=(Ad/Tk-Ad/Th)(1/S);
m1=.1001;

Solve[m1*9.81-(Pi*M^2*u*R^4)/4*(1/(z1)^2+1/(z1+2t)^2-2/(z1+t)^2)□0,z1]


u=4*Pi*10^-7;
R=.0254;
t=0.003174;
B=1.32;
M=(2*B/u);
Ap=Pi*(45/1000)^2;
Ad=Pi*(140/1000)^2;
Vcm=Pi*(45/1000)^2*(8/1000);
Vem=Pi*(145/1000)^2*(10/1000);
Pm= 500;
Tk=273+0;
Th=500+100;
S=Vem/Th+Vcm/Tk;
a=(Ap/Tk)(1/S);
b=(Ad/Tk-Ad/Th)(1/S);
m1=.1001;
F=1-a*(z2)+b*(0.09964981303487692`);
Solve[m1*9.81-(Pi*M^2*u*R^4)/4*(1/(z2)^2+1/(z2+2t)^2-2/(z2+t)^2)-Ap*Pm (1-
1/F)□0,z2]
```

```
function xp=Exp1(t,x)

%%% Masses %%%

md = 0.001; % mass of displacer
mp = 0.001; % mass of piston

mda = .1; % mass added to displacer
mpa = .1; % mass added to piston

mdt = md+mda; % total displacer mass
mpt = mp+mpa; % total piston mass

%%% Length %%%

ld= 21/1000; % length of displacer rod

%%% Area %%%

Ad= pi*(140/1000)^2; % Area of displacer
Ap= pi*(15/1000)^2; % Area of piston
Ak= pi*(150/1000)^2; %Area of cooler
Ah = pi*(150/1000)^2; %Area of heater

%%% Temperatures %%%

Th = 500+273; % Heater temperature
Tk = 0+273; % Cooler temperature

%%% Volumes %%%

Vcm = pi*(45/1000)^2*(10/1000); %Mean compression volume
Vem = pi*(145/1000)^2*(10/1000); %Mean expansion volume

S = Vem/Th+ Vcm/Tk; % Introducing new term
a = Ap/Tk * (1/S); % Placeholder
b = (Ad/Tk - Ad/Th) * (1/S); % Placeholder

%%% Pressures %%%

Pm = 101500; %Mean pressure;


%%% Magnets %%%

mu = 4*pi*(10^-7);
Bo = 1.3200; % Magnetic flux density value
R = 0.0254; % Radius of magnet
h = 0.003175; % Thickness of magnet
M = (2*Bo/mu); % Magnetization of magnet
mfield =(pi*mu*M^2*R^4)/4;
```

```
%%% Other %%%

g=9.81; %gravity
rho=1;
fl=0.05; %linear damping
fc=0.05; %cubic damping
kh=.05; %head loss

%%% EOMS %%%

xp=zeros(2,1);

Cf= 0.0457; % Fanning friction coeff;
n1= -0.2; %recommended by Martini;
Do= 152.4; %Outer diameter;
Di= 139.7; %Inner diameter;
dh = 4*0.25*pi*(Do^2-Di^2)/(pi*(Do+Di))/1000; %Hydraulic diameter for
annulus;
vis1=(181.94+0.536*(Th-293)+1.22*Pm)*10^-6; %Viscosity of air
vis2=(181.94+0.536*(Tk-293)+1.22*Pm)*10^-6; %Viscosity of air
L=10/1000;

dd=(pi*((Do/2)^2-(Di/2)^2)); %Area of annulus

e1=.0996755; % equilibrim pt for mass 1.
e2=.501; % equilibrim pt for mass 2.

utemp2 = (-2*Ad*x(2)+Ap*x(4))/dd;
utemp1 = (-2*Ad*x(2)+Ap*x(4))/dd;

%%%Model Fit%%%

xp(1)=x(2);
xp(2)=(Ad/mdt*((.5*rho*(ffcoef2*utemp2^n1+kh)*utemp2*abs(utemp2))...
    + (.5*rho*(ffcoef1*utemp1^n1+kh)*utemp1*abs(utemp1))))...
    +(mfield/mdt)*(1/(x(1)+e1)^2+1/(x(1)+e1+2*h)^2-2/(x(1)+e1+h)^2)-g;
xp(3)=x(4);
xp(4)=(Ap*Pm/mpt*(1-1/(1-a*(x(3)+e2)+b*(x(1)+e1))))-
(fl+fc*(x(3)+e2)^2)*x(4)/mpt+...
    (mfield/mpt)*(1/(x(3)+e2)^2+1/(x(3)+e2+2*h)^2-2/(x(3)+e2+h)^2)-g;
```

Bibliography

Banduric, R. D., and Chen N. J. C. (1984). Nonlinear Analysis of Stirling Engine Thermodynamics. *Oak Ridge National Laboratory Report*, 154.

Balachandran, B. and Magrab, E. (2003). Vibrations. *Cengage Learning.*

Benvenuto, G., and de Monte, F. (1995). Analysis of Free-Piston Stirling Engines/Linear Alternator Systems Part 1: Theory. *Journal of Propulsion and Power*, **11**: 1036-1046.

Benvenuto, G., and de Monte, F. (1995). Analysis of Free-Piston Stirling Engines/Linear Alternator Systems Part II: Results. *Journal of Propulsion and Power*, **1**:1047-1055.

Benvenuto, G., and de Monte, F. (1996). The Effect of Nonlinear Thermo-Fluid-Dynamic Terms on Free-Piston Stirling Machine Stability. *Proceedings of the 31st Energy Conversion Engineering Conference*, Washington, DC.

Benvenuto, G., de Monte, F., and Farina, F. (1990). Dynamic Behaviour Prediction of Free-Piston Stirling Engines. *Proceedings of the 25th Energy Conversion Engineering Conference.*

Berchowitz, D. M., and Redlich, R. W. (1985). Linear Dynamics of Free-Piston Stirling Engines. *Proceedings of the Institution of Mechanical Engineers*, **199**: 203-213.

Chen, N. J. C., and Griffin, F. P. (1983). A Review of Stirling Engine Mathematical Models. *Oak Ridge National Laboratory Report*, 135.

Chen, N. J. C., and Griffin, F. P. (1983). Linear Harmonic Analysis of Free Piston Stirling Engines. *Oak Ridge National Laboratory Report*, 172.

Chen, N. J. C., Griffin, F. P., and West, C. D. (1984). Linear Harmonic Analysis of Stirling Engine Thermodynamics. *Oak Ridge National Laboratory Report*, 155.

Choudhary, F. (2009). Dynamics of Free Piston Stirling Engines. *Master's Thesis, Department of Mechanical Engineering, University of Maryland, College Park, MD.*

Formosa, F. (2009). Nonlinear Dynamics Analysis of a Membrane Stirling Engine: Starting and Stable Operation. *Journal of Sound and Vibration*, **326**: 794-808.

Griffiths, D. J. (1999). Introduction to Electrodynamics. *Prentice Hall, Upper Saddle River, NJ.*

Ibrahim, M. B., and Tew, R. C. (2001). Study of Two-Dimensional Compressible Non Acoustic Modeling of Stirling Machine Type Components. *NASA Technical Memorandum 211066.*

Kankam, M. D., and Rauch, J. S. (1991). Comparative Survey of Dynamic Analyses of Free-Piston Stirling Engines. *NASA Technical Memorandum 104491.*

Kankam, M. D., and Rauch, J. S. (1993). Controllability of Free-Piston Stirling Engine/Linear Alternator Driving a Dynamic Load. *NASA Technical Memorandum 106497.*

Kankam, M. D., Madi, F. J., Rauch, J. S., and Santiago, W. (1992). A Free Piston Stirling Engine/Linear Alternator Controls and Load Interaction Test Facility. *NASA Technical Memorandum 105825.*

Martini, W. R. (1983). Stirling Engine Design Manual. *NASA Technical Memorandum 168088.*

Martini, W. R. (2001). Stirling Technology Development at GRC. *NASA Technical Memorandum 211315.*

Nayfeh, A. H. (1981). Introduction to Perurbation Techniques. *John Wiley and Sons, New York.*

Nayfeh, A. H. and Balachandran, B. (1995). Applied Nonlinear Dynamics: Analytical, Computational and Experimental Methods. *John Wiley and Sons, New York.*

Organ, A. J. (1992). Thermodynamics and Gas Dynamics of the Stirling Cycle Machine. *Cambridge University Press, UK.*

Organ, A. J. (1997). The Regenerator and the Stirling Engine. *Mechanical Engineering Publications Limited, London and Bury St Edmunds, UK.*

Senft, J. R., and Walker, G. (1985). Free Piston Stirling Engines. *Springer-Verlag, NY.*

Ulusoy, N. (1994). Dynamic Analysis of Free Piston Stirling Engines. *Ph.D. thesis, Department of Mechanical and Aerospace Engineering, Case Wester Reserve University, OH.*

Urieli, I., and Berchowitz, D. M. (1984). Stirling Cycle Engine Analysis. *Adam Hilger LTD., Bristol, NY.*

Urieli, I. (2010). Stirling Cycle Machine Analysis. *http://www.ohio.edu/mechanical/stirling/me422.html.*

Vokoun, D., Beleggia, M., Heller, L., and Sittner, P. (2009). Magnetostatic Interactions and Forces between Cylindrical Permanent Magnets. *Journal of Magnetism and Magnetic Materials.* **321**: 3758-3763.

Walker, G. (1980). Stirling Engines. *Clarendon Press, Oxford University Press, NY.*